J Mater Sci (2026) 61:26474–26496

Study on aging and overaging behavior of the AlSi9Cu3 alloy processed by PBF-LB

L. Tonelli[1,*], A. Martucci[2], I. Lagalante[2], L. Castagnini[1], M. L. Gatto[3,4], A. Morri[1], M. Cabibbo[3], M. Lombardi[2], and L. Ceschini[1]

[1] *Department of Industrial Engineering (DIN), Alma Mater Studiorum-University of Bologna, Viale del Risorgimento 4, 40136 Bologna, Italy*

[2] *Department of Applied Science and Technology (DISAT), Politecnico Di Torino, Corso Duca Degli Abruzzi 24, 10129 Turin, Italy*

[3] *Department of Industrial Engineering and Mathematical Sciences (DIISM), Università Politecnica Delle Marche, Via Brecce Bianche 12, 60131 Ancona, Italy*

[4] *Università degli Studi eCampus, Via Isimbardi 10, 22060 Novedrate (CO), Italy*

Received: 12 January 2026
Accepted: 13 June 2026
Published online: 17 July 2026

ABSTRACT

Al–Si–Cu alloys processed by laser-based powder bed fusion (PBF-LB) are promising candidates for lightweight high-performance automotive components, provided that post-processing heat treatments are developed to tailor their mechanical response. This study investigates the heat-treatment response and high-temperature stability of PBF-LB AlSi9Cu3 alloy, focusing on short-term direct aging treatments and a tailored T6 condition. Direct aging treatments (T5) were designed either to enhance strengthening (T5LowT) or to promote stress relieving (T5HighT), whereas the T6 (solutioning, quenching, and aging) was optimized by avoiding microstructure coarsening. The experimental approach included detailed microstructural characterization, residual stress measurements, and hardness tests before and after long-term exposure at 200–290 °C. The as-built (AB) alloy exhibited a high hardness of about 150 HB10, due to its extremely fine cellular solidification structure and supersaturated Al matrix, together with significant tensile residual stresses. The fine cellular structure was only marginally affected by T5 treatments, whereas it was significantly modified after T6. All treatments succeed in reducing the tensile residual stress (by 40% for T5 and completely after T6) and induced the precipitation of second phases. Approximately 160 HB10 was achieved after the T5LowT, while T5highT and tailored T6 treatments resulted in approximately 140 HB10. High-temperature exposure caused an overall hardness decrease in all investigated conditions, with a more pronounced and accelerated drop for T6 samples. The superior thermal stability of the AB and T5 conditions is attributed to the retention of the fine cellular structure, which acts as the most effective strengthening feature during high-temperature exposure.

Handling Editor: Nima Haghdadi.

Address correspondence to E-mail: lavinia.tonelli2@unibo.it

https://doi.org/10.1007/s10853-026-13203-y

Introduction

Currently, the necessity to enhance the sustainability and minimize the environmental footprint of crucial aspects of our society, such as public and private mobility, acts as a driving force for industrial and academic research [1–3]. In this context, one of the possible solutions relies on the increase in the efficiency of the propulsion system for road transportation. To this aim, from the material point of view, two main issues have to be addressed for the production of reliable structural components: (i) the selection of high-performance materials characterized by elevated mechanical strength (with particular emphasis on enhanced strength-to-weight ratios) and satisfactory physical properties, such as thermal stability and conductivity and (ii) the fabrication of highly customized components that minimize material utilization and, more importantly, waste [4, 5]. Both issues, if properly and concurrently managed, can lead to an overall lightweighting of vehicles, resulting in the reduction in energy consumption and harmful emissions [6]. The latter issue can be addressed by considering the application of innovative manufacturing routes, such as additive manufacturing (AM), that enable the production of engineered parts with a high degree of design complexity [7–9]. The powder-based laser bed fusion (PBF-LB), for example, is the most industrially developed AM technique that relies on the computer-driven melting of successive layers of metallic powder through a highly focused laser [10]. The result is weight-optimized components characterized by a peculiar microstructure due to the specific solidification conditions [11, 12]. The first issue, on the other hand, can be addressed by considering light alloys suitable to be processed by PBF-LB, such as Al–Si alloys [13, 14]. Among Al–Si alloys, the target could be represented by high-strength Al–Si–Cu alloys, like the AlSi9Cu3 alloy.

The AlSi9Cu3 is a heat-treatable alloy conventionally used for permanent-mold casting, usually processed by high-pressure die casting (HPDC) [15, 16]. As for other Al–Si cast alloys, it is mainly adopted to produce automotive components [17], also suitable for high-temperature applications [18]. Compared to other Al–Si alloys, the addition of copper to the alloy induces solid solution strengthening and enhances precipitation hardening thanks to the formation of θ-Al_2Cu reinforcing precursors (θ' and θ'') after a specific heat treatment, termed T6, consisting of solution treatment, quenching and aging [19]. For conventional Al–Si–Cu cast alloys, solution treatment is typically performed at 505–525 °C for 4–12 h, depending on the specific alloy composition, whereas artificial aging is commonly carried out at 155 °C for 2–5 h [20]. Al_2Cu reinforcing phases precipitate during the artificial aging phase from the supersaturated solid solution (Al_{sss}) obtained after solution treatment and quenching. θ'' coherent phase firstly forms from GP zones (consisting of cluster of Cu atoms) then, with prolonged aging, it evolves in the semi-coherent θ' phase and finally to the stable incoherent equilibrium phase θ-Al_2Cu (precipitation sequence: $Al_{sss} \rightarrow GP \rightarrow \theta'' \rightarrow \theta' \rightarrow \theta$). The maximum strengthening is obtained with the highest fraction of θ'' in the aged alloy (peak-aging condition) [19].

While the conventional cast alloy has been widely investigated, to the best of authors' knowledge, the state of the art regarding the characterization of the PBF-LB AlSi9Cu3 alloy consists of a few works [21–25]. To date, research has been focused mainly on: (i) optimization of the manufacturing process [21, 23]; (ii) in-depth microstructural characterization of the as-built (AB) alloy, also including phases characterization with the aid of X-ray diffraction (XRD) and transmission electron microscopy (TEM) analyses [22, 23]; (iii) mechanical characterization of the AB alloy, also by comparison with the conventional cast one [21, 22]; and (iv) study of the precipitation behavior and characterization of the alloy in selected heat-treated conditions [23–25]. As for the latter, works were focused on conventional T6 treatment [23, 24] and long-time annealing treatment (up to 64 h) carried out at low temperature (140–180 °C) to induce aging of the alloy [24] or relatively high temperature (250 and 300 °C) to induce relief of residual stress [24, 25]. From the study of the current state of the art, it emerges that the alloy processed by PBF-LB is characterized by interesting mechanical properties, especially if compared to the conventional cast alloy, thanks to the extremely fine microstructure and supersaturation condition resulting from PBF-LB, as well as to a lower defect content when compared to the HPDC alloy. As for other Al–Si alloys processed by PBF-LB, the AlSi9Cu3 one in the AB state displays a cellular solidification structure composed of submicrometric α-Al cells surrounded by a fine interconnected network of eutectic Si with trace of Al_2Cu segregated at cells borders [22, 23]. At very high magnification, such network appears to be composed of a high density of cubic Si particles (with a size ranging from 30 to 70 nm) able to hinder dislocation movement [22]. The overall good mechanical performance is preserved also after the selected heat-treatment conditions so far considered in the literature, thanks to the precipitation of Al_2Cu precursors and nanometric Si within Al cells [23–25]. However, it is authors' opinion that there is a substantial lack of references on short-term aging treatment, which can represent an interesting opportunity to shorten the time-to-market and to boost energy saving, resulting in the enhancement of industrial feasibility. Short-term treatment carried out from the AB alloy, typically referred to as T5 treatments, can be tuned to enhance strengthening of the alloy or stress relieving, as evidenced in the literature for long-term ones. Furthermore, the potential of an innovative T6 treatment specifically tailored to the peculiar microstructure of PBF-LB alloys has not yet been explored. Such a treatment could preserve microstructural fineness by reducing the holding time and optimizing the treatment temperature. Although T6 treatments have already been investigated in the literature for the Al–Si–Mg systems, most studies have mainly focused on AlSi10Mg and AlSi7Mg alloys [13, 14]. The addition of Cu modifies the precipitation behavior and therefore requires a dedicated investigation of the heat-treatment response. Furthermore, for AlSi9Cu3 alloy, the available literature has so far mainly addressed the effect of conventional T6 treatments [24, 25], i.e., treatments based on the microstructural features of cast alloys, which differ significantly from those of PBF-LB materials. A tailored T6 treatment could instead improve the trade-off between strength and ductility, as already shown for AlSi10Mg and AlSi7Mg alloys [26]. It should also be considered that no mention was made to the thermal stability of this alloy. In this alloy, the presence of Cu leads to the formation of Cu-based intermetallic phases with an improved thermal stability if compared to Al-Si heat-treatable alloys such as AlSi7Mg that suffers a decrease in the mechanical properties (especially hardness and tensile strength) in case of exposure at temperature > 200 °C, due to the coarsening of reinforcing precipitates [27]. Thermal stability is enhanced especially in case of the quaternary Al–Si–Cu–Mg alloys where the quaternary Q-phase is formed [28–30]. For the conventional heat-treated Al–Si–Cu cast alloys, the stability of the aging precipitates (θ-Al_2Cu and eventually Q–$Al_5Cu_2Mg_8Si_6$ in presence of Mg) is responsible for the overall satisfying high-temperature behavior [31–33]. Their thermal stability is limited by the high diffusivity of Cu (and eventually Mg) occurring at high temperatures. At 300 °C, the diffusivity of Cu rises rapidly and both phases become thermodynamically unstable, leading to modifications of precipitate size and shape [32]. According to [31], θ-Al_2Cu should retain its stability up to 280 °C, while Q–$Al_5Cu_2Mg_8Si_6$ can face temperatures above 300 °C. However, as the microstructure of the PBF-LB alloy is considerably different from the cast one even after heat treatment and, as previously discussed, can rely on different reinforcing precipitates according to the selected heat treatment, the characterization of the response to high-temperature exposure (i.e., overaging behavior) should be included in the literature.

Therefore, the present study aims to broaden the understanding of the response to heat treatment of the AlSi9Cu3 PBF-LB alloy by considering: (i) short-term direct aging treatments (T5 treatments) optimized to boost either strengthening or stress relieving; (ii) an innovative T6 treatment specifically tailored on the peculiar PBF-LB microstructure; (iii) the response to high-temperature long-term exposure (overaging behavior) of the alloy in the AB state and after the optimized heat treatments (T5 and T6). Finally, the hardness evolution due to thermal exposure was monitored to assess the mechanical response of the alloy.

Experimental procedure

Production of PBF-LB samples

A commercial gas-atomized AlSi9Cu3(Fe) powder provided by ECKA Granules Germany GmbH, with a reported size range of 20–63 µm, was chosen to produce samples. The powder chemical composition is reported in Table 1 where data provided by the supplier are compared to the chemical composition obtained by glow-discharge optical emission spectroscopy (GD-OES, GDA 650, Spectruma Analytik GmbH) on the PBF-LB samples. By referring to data in Table 1, it is possible to conclude that both powder and produced samples adhere to the compositional range specified in standard EN1706:2020 and ASTM B108/108 M for the alloy ENAC-46000 and A333, respectively.

The particle size distribution (PSD) of the powder was measured through laser diffraction particle size analyzer resulting in D10 = 7.9 µm, D50 = 45.3 µm and

Table 1 Chemical composition of AlSi9Cu3 PBF-LB samples as analyzed by GD-OES and compared to composition provided by powder supplier and range given by standards

	Element %wt							
	Si	Cu	Fe	Mg	Mn	Zn	Other	Al
Supplier powder data sheet	9.3	3.0	0.91	0.29	0.21	0.81	–	Bal
GD-OES on produced samples	8.84 ± 0.08	2.78 ± 0.01	0.72 ± 0.01	0.28 ± 0.01	0.21 ± 0.01	0.72 ± 0.04	0.03	86.43 ± 0.04
EN 1706:2020 (ENAC-46000)	8.0–11.0	2.0–4.0	0.6–1.1	0.05–0.55	0.55 max	1.2 max	–	Bal
ASTM B108/108 M (A333)	8.0–10.0	3.0–4.0	1.0 max	0.05–0.50	0.5 max	1.0 max	–	Bal

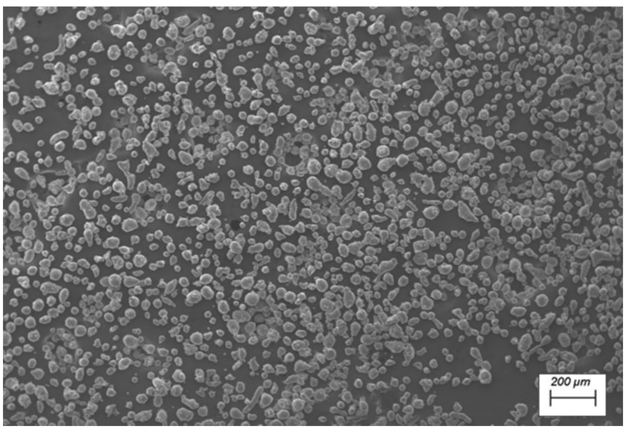

Figure 1 AlSi9Cu3 powder morphology observed by SEM.

D90 = 68.4 μm. Image analysis through SEM allowed the evaluation of the powder morphology (Fig. 1). Powder particles appeared overall regularly shaped with a limited number of satellites spotted.

Samples were produced using an EOSINT M270 dual-mode system (EOS GmbH) under an argon atmosphere, with an aluminum build platform maintained at 100 °C throughout the process. A preliminary design of experiments was carried out to investigate the influence of laser power (170–195 W), scan speed (800–1400 mm/s), and hatch distance (0.10–0.14 mm), while keeping the layer thickness constant at 30 μm. Based on porosity measurements obtained via the Archimedes method, samples produced with a laser power of 170 W consistently exhibited higher porosity levels compared to those processed at 195 W. Therefore, the lower power condition was excluded from further optimization.

Subsequently, the experimental data at 195 W were analyzed using computer-aided tuning (CAT) software to identify the optimal combination of hatch distance and scan speed. The optimization aimed at minimizing porosity and reducing lack-of-fusion defects, particularly in view of subsequent fatigue testing. The optimal parameter set, as shown in Fig. 2, was identified as: laser power 195 W, scan speed 800 mm/s, and hatch distance 0.14 mm.

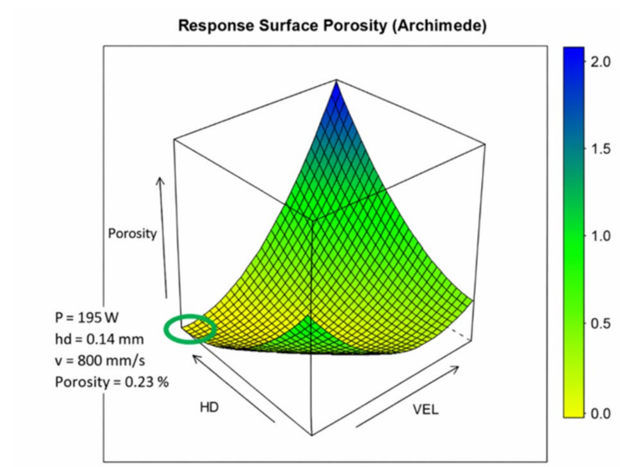

Figure 2 Process optimization for PBF-LB of the AlSi9Cu3 alloy: response surface of porosity as a function of hatch distance, scan speed at a laser power of 195 W, obtained using CAT software.

Porosity was evaluated using both the Archimedes principle and image analysis, yielding values of 0.23 ± 0.11% and 0.46%, respectively. For the gravimetric measurements, a reference density of 2.76 g/cm^3, as provided in the powder datasheet, was assumed as the fully dense condition. Cubes sized 10 × 10x10 mm^3 were built for material characterization and heat-treatment optimization.

Phase composition, residual stress, and thermal analysis

A thorough characterization has been carried out on both AB and heat-treated conditions to assess the response of the PBF-LB alloy to a high-temperature exposure and therefore tailor the post-processing heat treatments.

The thermal response of the alloy was recorded through differential scanning calorimetry (DSC) using a 214 Polyma, with the response to heating documented from 25 to 550 °C. The heating rate was set at 20 K/min for as-built and heat-treated samples. Samples were inserted in alumina crucibles, and the measurements were performed in a nitrogen atmosphere.

To further investigate the different phases, XRD analysis was conducted using a PANalytical X'Pert PRO PW3040/60 diffractometer, and peaks were analyzed using the X'Pert HighScore software. The measurements were performed with Cu-Kα1 radiation over an angular range of 2θ from 10 to 150°, with a step size of 0.013° and a step time of 60 s.

Residual stresses were also recorded through a Pulstec µ360x operated at 30 kV with a chromium cathode. Five measurements per face were collected, moving from the bottom of the sample toward the top along the building direction.

Microstructural characterization

Specimens for microstructural characterization were extracted from cubic samples perpendicularly to the building direction (transversal section). Metallographic preparation involved embedding the specimens in a conductive resin, grinding with abrasive papers, and polishing up to 1 µm polycrystalline diamond suspension, following standard metallographic procedures [34, 35].

To reveal the microstructural features, chemical etching was carried out using Weck's reagent (3 g NH_4HF_2, 4 mL HCl, 100 mL distilled water) through a 10 s immersion at room temperature.

A field emission-gun scanning electron microscope (FEG-SEM, Tescan Mira3) operating at 10 kV and equipped with energy-dispersive spectroscopy (EDS) for semiquantitative localized chemical analyses was used to investigate the main microstructural features at high magnification.

For transmission electron microscopy (TEM) thin disks were mechanically ground and thinned down to a thickness of 80–90 µm, then punched and dimpled to a thickness of ~ 30 µm, and finally ion milled to electron transparency by a Gatan© PIPS working at 8 keV, with incident beam angle progressively reduced to 8, 6, and 4°. TEM inspections were carried out using a Philips© CM-20® working at 200 keV using a double-tilt specimen holder cooled with liquid nitrogen.

Heat treatments for aging and overaging characterization

The optimization of heat-treatment parameters is essential to achieve the desired strength for the specific structural applications within an industrially viable timeframe. In this study, PBF-LB samples were subjected to two distinct heat-treatment protocols: (i) direct artificial aging from the AB condition (T5 treatment) and (ii) solution treatment and water quenching followed by artificial aging (T6 treatment). The investigated heat-treatment parameters, including temperature and duration, are summarized in Table 2.

To optimize post-processing heat treatments, aging curves were developed from hardness measurements carried out on samples subjected to artificial aging (AA). Brinell tests were performed with a 62.5 kg load and a 2.5 mm-diameter hardened steel ball indenter (HB10) [36], following the temperature–time combinations detailed in Table 2. These aging curves present hardness values as a function of aging time and temperature, enabling the identification of the peak-aging condition (both time and temperature) at which the alloy reaches its maximum hardness. Four temperatures, at 20 °C intervals (160 °C, 180 °C, 200 °C, 220 °C), were evaluated over a 6 h holding period to ensure industrial feasibility. The temperature selection was

Table 2 Heat-treatment conditions investigated in the present study for the AlSi9Cu3 PBF-LB alloy

Heat-treatment conditions					
Heat treatment	Solution treatment (ST)		Quenching (WQ)	Artificial aging (AA)	
	T [°C]	t [min]		T [°C]	t [h]
T5	–	–	–	160	0.5
				180	1
				200	2
				220	3
					4
					6
T6	505	15	Warm water (25–30 °C)	160	0.5
		30		180	1
		60		200	2
				220	3
					4
					6

guided by DSC analysis conducted on AB samples, as will be later discussed. Aging curves were elaborated for both T5 and T6 treatments. In case of T5 treatment, the curves describe the response to AA starting from the AB alloy. On the other hand, in case of T6, this response is studied on solution-treated and quenched samples. Therefore, the optimization of the T6 heat treatment was carried out in two stages: (i) optimization of the solution treatment (ST) parameters, followed by (ii) optimization of AA conditions, as shown in Table 2. The solution treatment temperature was set at 505 °C based on both an extensive review of the literature [20, 37–39] and DSC analysis. Furthermore, with regard to ST duration, as reported by other authors [40, 41] a shorter time is more suitable for PBF-LB samples than the conventional 8 h typical for cast aluminum alloys, as it reduces undesirable grain coarsening and porosity growth. Accordingly, a single-stage ST was performed at 505 °C for 15, 30, and 60 min, followed by water quenching (WQ) in warm water (25–30 °C). Microstructural characterization and Brinell hardness tests were performed on ST + WQ samples to identify the optimal solution treatment condition. Building upon these findings, the subsequent optimization of aging parameters was performed using the best solution treatment and quenching conditions. Notably, for both T5 and T6 at 160 °C hardness continued to increase after 6 h exposure, hence, for the sake of completeness, the response to AA was studied up to 16 h for the 160 °C curve. The optimized aging conditions were further validated through DSC and XRD analyses on heat-treated samples.

Since the alloy can experience temperatures higher than that of peak aging during the in-service life, the overaging (OA) behavior was also evaluated. Hardness variation (HB10) was analyzed as a function of time and temperature for exposure duration up to 72 h at 200, 245, and 290 °C, for both T5 and T6 heat-treated samples. The OA conditions were selected to simulate the working conditions that mechanical parts, such as high-performance motorcycle engine components, are expected to face during their in-service life. Specifically, these conditions accounted for the average operational temperature (200 °C) and peak temperatures (245 and 290 °C) experienced during races [42].

For both AA and OA, the hardness–time–temperature curves were obtained using a Binder electric furnace with a maximum temperature of 300 °C. ST were instead performed in a Nabertherm electric furnace capable of reaching 1200 °C. Both furnaces were equipped with thermocouples and a data logger, ensuring temperature stability within ± 5 °C.

Results

Characterization of the as-built alloy

The PBF-LB process is characterized by high-speed cooling rates and significant thermal gradients, which greatly affect the final microstructure of the produced alloy. Indeed, many studies have reported a peculiar and extremely fine AB microstructure in aluminum alloys, enhanced by rapid cooling [43–45]. At lower magnification, an overview of the very fine cellular structure characterizing the AB alloy can be observed (Fig. 3a). Such cellular structure consists of a dense eutectic Si-rich network surrounding a α-Al matrix, as evidenced by EDS analyses in Fig. 4 and as also reported in the literature [22]. In Fig. 3a, the three main regions already described for other Al–Si alloys [46] can be distinguished: melt pool core (MPC, yellow frame in the figure), melt pool border (MPB, orange frame in the figure), and heat-affected zone (HAZ, red frame in the figure). These zones are characterized by different thermal history that affects the morphology of the cellular structure, as can be clearly observed at higher magnification. MPC preserves the finest microstructure with an interconnected Si network (Fig. 3b). Coarsening of the cellular structure and partial cracking of the Si network occur in the MPB (Fig. 3c), while a discontinued Si network characterizes the HAZ (Fig. 3d). In the area of the Si network, the presence of Cu compounds in the network along with Si has been observed by Fousava et al. [22]. Indeed, EDS analyses in Fig. 4 show a slightly higher content of alloying elements in the proximity of the Si-rich network (points 3 and 4). The high cooling rates not only refine the microstructure, resulting in the peculiar cellular network, but also limit the formation of phases, leading to a supersaturated solid solution.

The occurrence of supersaturation was also confirmed by further analyses (XRD and DSC). XRD of the AB material showed indeed mainly peaks related to Al (Fig. 5a). Only a few minor phases with small intensities, associable with Si and Al_2Cu phases, could be observed, corroborating the idea that most elements are still in solid solution and only minor

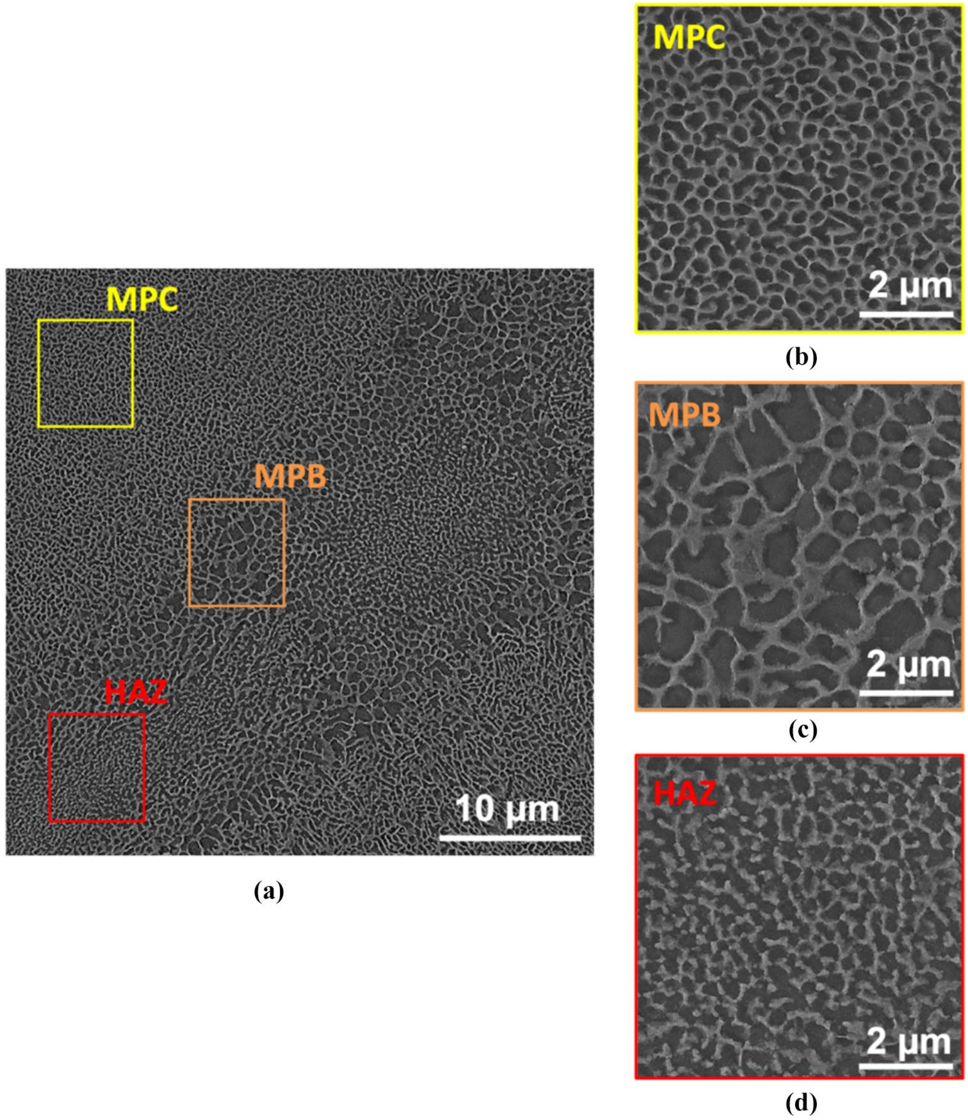

Figure 3 Microstructural features of the AlSi9Cu3 PBF-LB AB alloy characterized by FEG-SEM: **a** low-magnification overview of the cellular structure; **b**, **c**, and **d** high-magnification details of the melt pool core (MPC), melt pool border (MPB), and heat-affected zone (HAZ), respectively. Micrographs refer to the transversal section (perpendicular to the building direction).

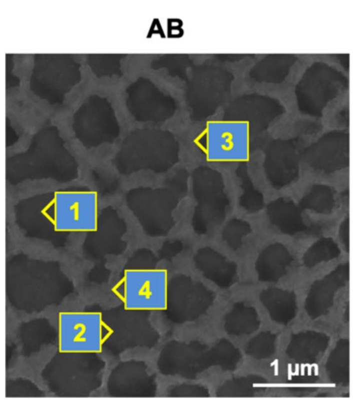

Normalized mass concentration [%]

	Al	Si	Cu	Fe	Mg
1	87.77	8.07	3.06	1.09	0.01
2	87.62	9.39	2.91	0.01	0.07
3	70.89	22.59	5.06	1.23	0.23
4	68.44	24.61	5.11	1.64	0.20

Figure 4 EDS semiquantitative analyses on the cellular structure of the AlSi9Cu3 PBF-LB AB alloy showing the distribution of main alloy elements in the MPB region. The analyses refer to the transversal section (perpendicular to the building direction).

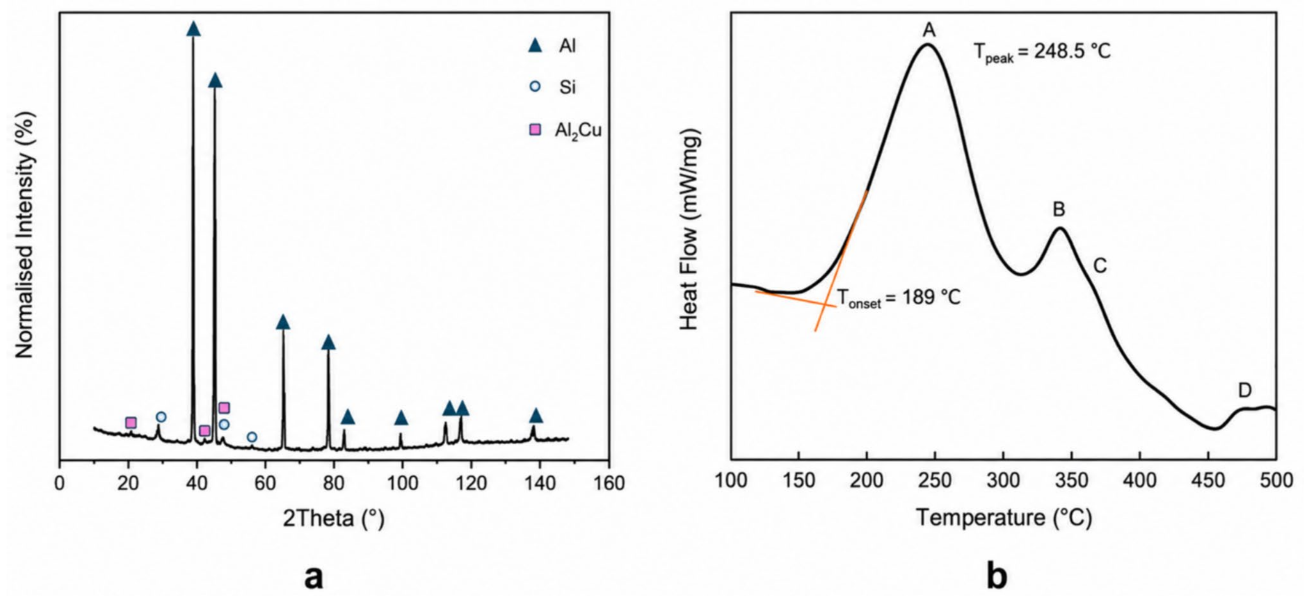

Figure 5 Characterization of the AlSi9Cu3 PBF-LB AB alloy: **a** XRD spectrum; **b** DSC curve.

phases have already precipitated, in accordance with previous studies [22, 24].

During heating of the AB alloy, four main thermal events were identified in the DSC curve, labeled as A, B, C, and D in Fig. 5b. The first and most intense peak, peak A, showed an onset temperature of 189 °C and a peak temperature of 248 °C. This event was mainly associated with Si precipitation from the supersaturated α-Al matrix, although a contribution from the early formation of Cu-rich metastable precipitates, such as θ'', cannot be excluded, since these transformations may partially overlap in this temperature range.

Peaks B and D were associated with the subsequent precipitation sequence of Al_2Cu-related phases, with peak B attributed to θ' precipitation and peak D attributed to the formation of the more stable θ phase. Peak C was instead related to the spheroidization/coarsening of the previously precipitated Si phase. These outcomes are consistent with the DSC scan reported by Fiocchi et al. for a comparable Al–Si–Cu composition [23]. In addition, as reported in [47], the high-temperature peak D may also include a contribution from Al–Fe phase precipitation in Al–Fe–Si–containing alloys.

Overall, the DSC analysis indicates that a significant fraction of Si and Cu remain in supersaturated solid solution in the AB condition, since the main precipitation reactions occur during heating. Therefore, the DSC results provide useful support for interpreting the alloy response during the investigated heat treatments.

Heat-treatment response assessment

Direct aging—T5 treatment

Artificial direct aging from the metastable and supersaturated PBF-LB alloy can be exploited with a twofold objective: (i) induce strengthening of the alloy thanks to the precipitation of reinforcing particles from the supersaturated matrix and (ii) partial relief of the tensile residual stress that usually characterizes the AB condition. With this in mind, the response to direct aging of the AlSi9Cu3 alloy was investigated by drawing aging curves (Fig. 6a) representing the evolution in hardness after the exposure at different aging temperatures for a given time. The investigation considered an exposure time up to 6 h to preserve a short-time treatment with the aim of promoting its industrial feasibility and limiting the energy consumption. Aging temperatures were chosen based on DSC performed on the AB alloy (Fig. 5b) to fall within the main precipitation peak occurring, according to the DSC spectrum, in the range approximately 180–250 °C. Therefore, four temperatures with a 20 °C gap were chosen in the range 160–220 °C (160, 180, 200, 220 °C).

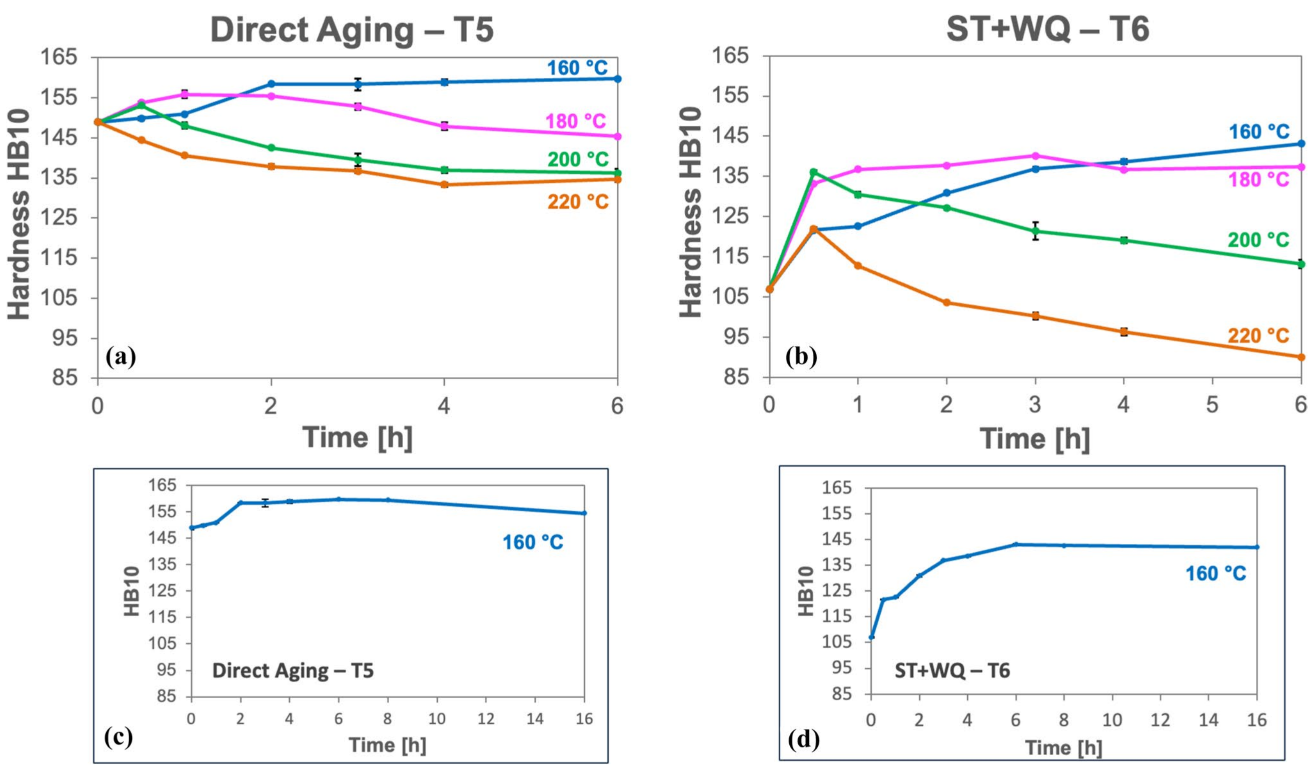

Figure 6 Aging curves describing the evolution of hardness (mean value and error bars) as a function of temperature (160, 180, 200, 220 °C) and time (up to 6 h) for the AlSi9Cu3 PBF-LB alloy: **a** direct aging of the AB alloy (T5 treatment); **b** aging of the ST + WQ alloy (T6 treatment). In the insets: 160 °C aging curve up to 16 h for both T5 **c** and T6 **d**.

Low-temperature direct aging (160 and 180 °C) induced strengthening of the alloy, especially in case of 160 °C treatment. In fact, peak aging was obtained between 3 and 6 h exposure at this temperature, reaching a hardness value of about 159 HB10 (+ 7% compared to AB). To make sure that the hardness peak was effectively reached, only for the 160 °C treatment, the aging curve was drawn up to 16 h (Fig. 6c), proving that the peak hardness was maintained up to 8 h and then slightly decreased to 154 HB10 after 16 h exposure. High-temperature aging treatment (200 and 220 °C), instead, induced a substantial softening in the alloy, with the sole exception of 30 min exposure at 200 °C. However, the maximum drop in hardness was rather restrained as it was reached at 4–6 h exposure with a value of about 134 HB10 (− 10% from AB).

Definition of solution treatment (ST) conditions

The definition of the optimized ST conditions to be applied was based on both literature review and experimental results. In fact, two main issues have to be taken into account: (i) Al-Cu alloys may experience incipient melting of Al_2Cu compounds, which is often avoided by applying a two-stage ST [19]; (ii) excessive microstructure coarsening due to exposure at high temperature during ST may occur. These issues were addressed by optimizing both treatment time and temperature. In particular, DSC of the AB alloy in Fig. 5b showed no trace of incipient melting; therefore, a two-stage ST can be replaced by a single-stage one. Also, the ASTM B917/B917M standard suggests for the A333 (Al–Si–Cu permanent-mold casting alloy) a single-stage ST at 505 °C [20]. Furthermore, according to the well-established literature on the A319 conventional cast alloys [37, 38], 505 °C can be considered a safe temperature for a single-stage ST. The temperature of incipient melting of Al_2Cu seems to be strictly related to Mg content (it decreases with increasing Mg%), particularly if Mg > 0.6% [37]; the alloy utilized in the present study has Mg < 0.3%, as verified by GD-OES analyses on the produced samples (Table 1).

Based on the above, a single-stage ST at 505 °C was selected. Treatment time, on the other hand, was chosen following microstructural and hardness evaluation

(Fig. 7). To avoid excessive coarsening and porosity formation that might occur during solution treatment of PBF-LB Al alloys, the maximum solution treatment time was set at 60 min, and intermediate durations (15 and 30 min) were also considered. Results show that even the shortest ST (Fig. 7b) induced the complete breakdown of the typical cellular structure that characterizes the PBF-LB AB alloys (Fig. 7a), consisting of α-Al cells surrounded by a fine and interconnected Si-rich network, as discussed in the previous section. As evidenced by EDS analyses in Fig. 8, the microstructure of ST + WQ samples consists of a composite-like structure in which Si-rich globules, originated from the Si-rich network, are surrounded by the Al matrix. The occurrence of Si network breakdown after solution treatment is also supported by previous studies, where this phenomenon has been extensively documented for AlSi7Mg and AlSi10Mg alloys [40, 41, 44]. Microstructural features of heat-treated alloy will be in-depth discussed in the following Section. At this stage, the focus is driven to avoid excessive coarsening of Si-rich globules, which were significant only after the 60 min treatment. The 15- and 30 min treatments, on the other hand, were quite comparable in terms of

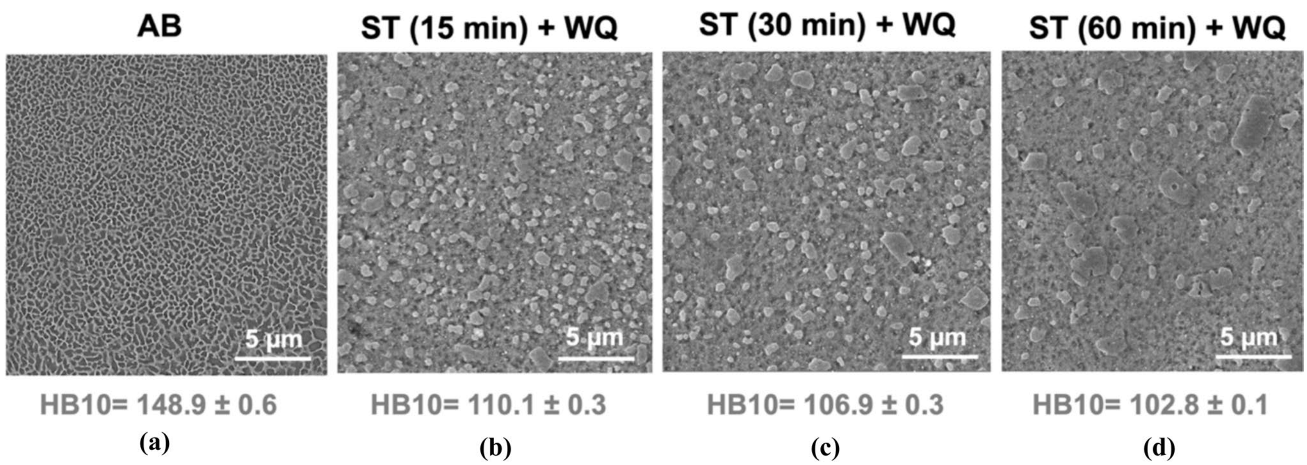

Figure 7 Microstructural analyses and hardness data (HB10) for the AlSi9Cu3 PBF-LB AB alloy **a** compared to the alloy after solution treatmentat 505 °C for: **b** 15 min, **c** 30 min, **d** 60 min followed by water quenching.

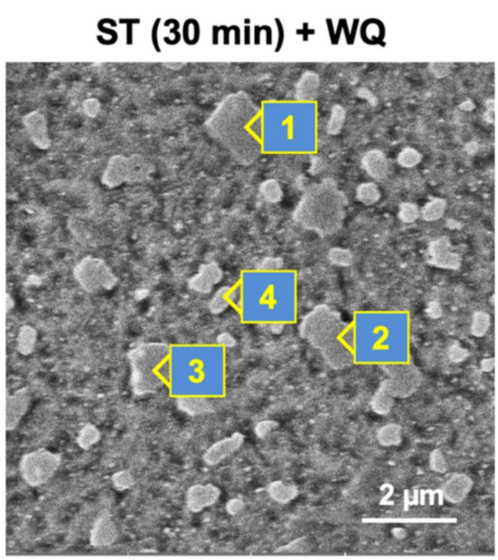

	Normalized mass concentration [%]				
	Al	Si	Cu	Fe	Mg
1	11.35	85.81	1.38	1.44	0.02
2	11.19	86.68	1.19	0.84	0.10
3	28.69	68.14	1.74	1.29	0.14
4	65.52	29.42	3.59	1.16	0.31

Figure 8 EDS semiquantitative analyses of globular particles formed in the AlSi9Cu3 alloy after solution treatment and quenched under the condition selected for further investigation (ST 30 min + WQ).

finesse and homogeneous distribution of globules. In terms of hardness, all treatments resulted in a decrease if compared to the AB condition, but the variation among the performed ST treatments is rather reduced. Therefore, in view of possible industrial applications, the treatment time of 30 min was selected to promote the effectiveness of the ST treatment even in case of complex and medium-to-large components.

T6 treatment

In the most recent literature of PBF-LB Al alloys, the complete treatment consisting of ST + WQ + AA (T6 treatment) was proved to be the best choice to increase the overall mechanical performance of the alloy, by enhancing the trade-off between strength and ductility [48–51]. Therefore, even if T6 treatment is a multiple-stage treatment involving also an exposure at high temperature and its industrial applicability can be questioned by reason of energy savings, this type of treatment was also taken into consideration. To optimize the artificial aging step, aging curves (Fig. 6b) were repeated, considering the same temperatures and times as for T5 treatment, on samples subjected to the selected ST + WQ treatment. As for direct aging, results show that low-temperature aging treatments (160 and 180 °C) succeed in inducing strengthening. The maximum value of about 140 HB10 (+ 29% from ST + WQ condition and- 7% from AB) was reached even after a 1 h exposure in case of 180 °C treatment and 4 h at 160 °C. At 180 °C, the maximum hardness was maintained up to 3 h and then slightly decreased for the 6 h exposure. In case of 160 °C, long treatment time (from 6 to 16 h, Fig. 6d) led to slightly higher hardness values (approximately 143 HB10). However, this mild difference cannot be considered significant enough to justify a more than doubled aging treatment time. Concurrently, high-temperature aging (200 and 220 °C) after an initial strengthening resulted in alloy softening as the exposure time increases, leading to a more significant drop in hardness than the T5 treatment. The minimum value of about 90 HB10 (− 16% from ST + WQ condition) was reached in case of 220 °C.

Based on the discussed results, the optimized heat-treatment conditions were defined as reported in Table 3. Other than the AB condition that will act as a benchmark for detailed microstructural analyses to assess the effect of heat treatment and overaging, three different heat-treatment conditions were considered: (i) direct aging at low temperature (T5LowT), (ii) direct aging at high temperature (T5HighT), and (iii) T6 treatment. T5LowT and T6 heat treatments were selected in the peak-aging condition, to promote alloy strengthening. For the T6 treatment, both 160 and 180 °C aging conditions led to maximum hardness values. However, the 180 °C condition was selected because it allowed the aging time to be reduced by half. In view of potential industrial applications, a 2 h treatment was chosen to ensure adequate treatment homogeneity, even in large components, while maintaining a moderate overall processing time. The T5HighT treatment instead was selected as a short-time treatment able to reduce the tensile residual stress and possibly promote the trade-off between strength and ductility by comparison to AB, by reason of a slight decrease in alloy hardness (− 7% compared to AB) that is also comparable to T6.

Table 3 Summary of optimized heat-treatment conditions considered for microstructural analyses and characterization of overaging behavior of the AlSi9Cu3 PBF-LB alloy

	Optimized heat-treatment conditions				
	Solution Treatment		Quenching	Artificial aging	
	T [°C]	*t* [min]		T [°C]	t [h]
AB	–	–	–	–	–
T5LowT	–	–	–	160	3
T5HighT	–	–	–	220	1
T6	505	30	Warm water (25–30 °C)	180	2

Characterization of the heat-treated alloy

The hardness variations described by the aging curves are closely related to microstructural changes occurring during the heat treatment, such as precipitation, precipitate growth, and possible overaging phenomena. Therefore, an in-depth investigation of microstructural evolution induced by heat treatment was carried out on the optimized conditions defined in Table 3, with AB alloy as reference.

In this work, XRD, DSC, and residual stress analyses supported and guided the definition of optimized heat treatment and corroborated the microstructural observation that will be discussed in the following.

The DSC curves highlighted the different Si precipitation behavior after each heat treatment (Fig. 9). Indeed, the sample subjected to T5LowT showed the same peaks already observed for AB. The first peak (defined as peak A in Fig. 5b) related to the precipitation of θ'' and Si from the supersaturated Al matrix showed a reduced intensity, suggesting that minor precipitation occurred. On the other hand, some more evident differences could be observed after the T5HighT. Indeed, the same peak disappeared, indicating that complete precipitation occurred during the heat treatment, while the second peak related to θ' formation (defined as peak B in Fig. 5b) was preserved. Finally, after T6, both exothermic peaks (A and B) were replaced with one sole peak, possibly associated with the precipitation of the Cu that had remained in solid solution and was yet to precipitate.

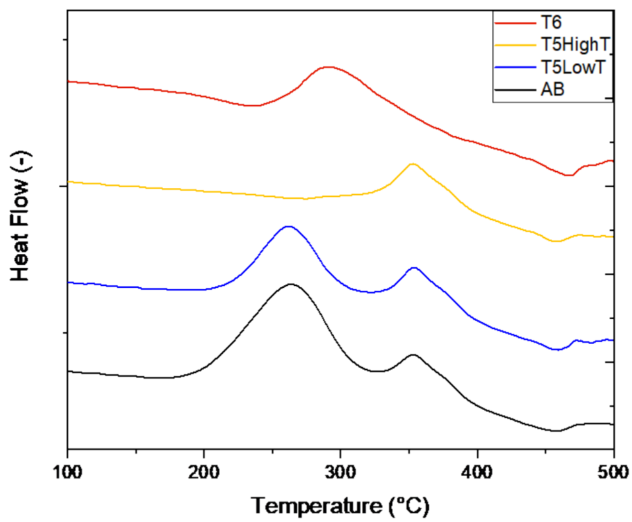

Figure 9 DSC of the AlSi9Cu3 PBF-LB heat-treated alloy (T5LowT, T5HighT, and T6) compared to AB.

XRD analysis further deepened the understanding of the effects of heat treatments on the microstructure (Fig. 10). After T5LowT and T5HighT, the XRD analyses showed no significant differences compared to the AB condition. They mainly displayed Al peaks with a few minor peaks, mostly related to Si and Al_2Cu. However, after T6, more differences were observed. Si peaks became more pronounced, indicating the presence of larger phases after the treatment, which allowed a more intense signal. Additionally, a few new peaks appeared, mainly attributed to minor phases with Cu and Fe, like N-phase Al_7Cu_2Fe. However, these peaks were not very intense, probably due to their small size and low content in the material, and other peaks related to their pattern could be hidden by the more intense Si and Al peaks.

It is interesting to notice that the Al peaks tended to shift toward smaller angles after each heat treatment, with the most significant shift after T6. According to Bragg's law, i.e., $n\lambda = 2d\sin\theta$ (where λ is the X-rays wavelength, d the interplanar spacing, and θ the angle of incidence), a shift toward lower diffraction angles corresponds to an increase in the interplanar spacing and therefore to a variation in the lattice

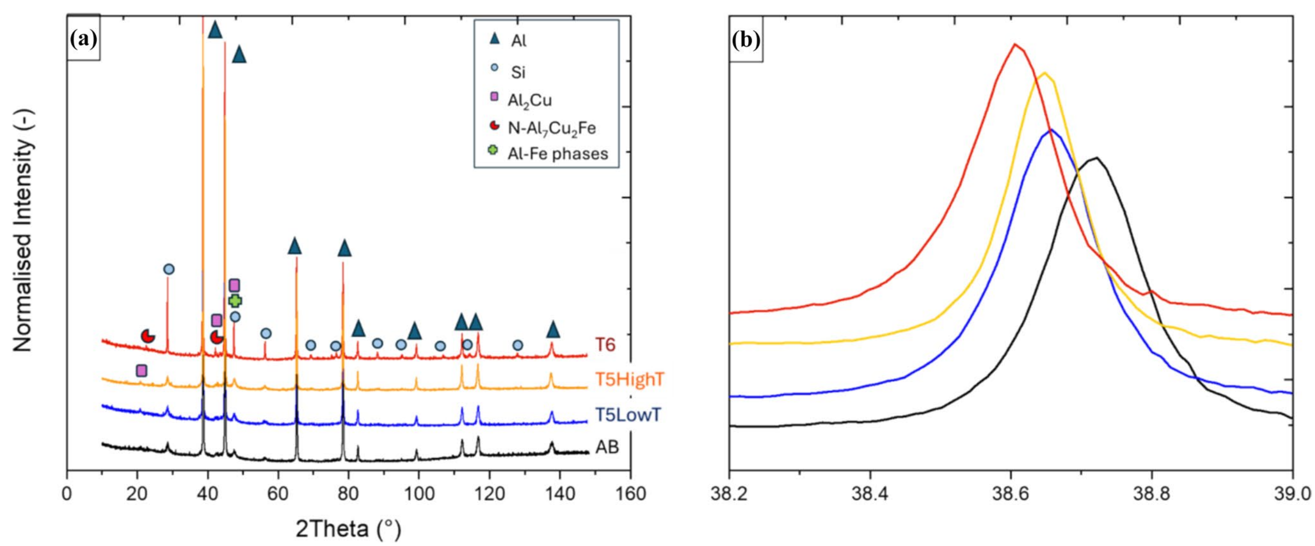

Figure 10 Phases analysis (XRD) of the AlSi9Cu3 PBF-LB heat-treated alloy (T5LowT, T5HighT, and T6) compared to AB: **a** complete spectra, **b** detail on peak around 38°.

parameter of the Al matrix. When alloy elements are in solid solution, they tend to increase or decrease the lattice parameter, depending on their atomic radius in comparison with Al [52, 53]. In Al-based alloys, the precipitation of solute elements such as Cu, Si, and Fe, which have smaller atomic radii than Al, may contribute to an increase in the lattice parameter of the Al matrix due to the depletion of the supersaturated solid solution. However, this effect cannot be considered independently from the residual stress state, since residual stresses may also affect the measured interplanar spacing and therefore the peak position. For this reason, residual stress measurements were performed and are reported in Fig. 11. An analogous outcome was already observed in a previous work of the authors for the AlSi7Mg alloy [54].

The rapid cooling rates and complex thermal gradients to which the material is subjected during the process also create undesirable tensile stress that negatively affects the mechanical behavior. However, heat treatments can be performed to release these stresses [55, 56]. Among heat treatments, also aging has been reported as able to reduce residual stress, though without being able to completely release it [57]. On the other hand, higher temperatures used in treatment like ST can fully release all the tensile residual stresses, while greatly modifying the microstructure and homogenizing it. As a result, ductility significantly improves, also resulting in a more uniform behavior without excessive variation in the building direction, getting rid of the anisotropy typical for PBF-LB alloys [58, 59]. The data reported in Fig. 11 are consistent with literature evidence. The highest stresses were found in the AB sample, whereas a slight release of the stresses was recorded after the T5 treatments, though without any major difference between T5LowT and T5HighT. After T6, the measured residual stress decreased to − 13.0 ± 8.0 MPa, indicating the complete relaxation of the tensile residual stresses generated during PBF-LB and the development of a slight compressive stress state. This slightly compressive value is mainly attributed to the quenching step following solution treatment. Indeed, rapid cooling can induce thermal gradients and differential contraction between the surface and the inner regions of the sample, leading to near-surface compressive residual stresses. Since the measurements were performed by XRD, the obtained values are representative of the near-surface stress state. Therefore, the compressive residual stress after T6 should be mainly interpreted as a quenching-induced effect, rather than as a direct consequence of phase transformation. It is worth noting that in addition to the release of the stresses, the standard deviation is noticeably smaller in the T6 sample compared to all other conditions. This results from the homogenization of the microstructure, decreasing the anisotropy and leading to more consistent material behavior. It must also be noted that residual stresses were measured on samples after removal from the building platform using electrical discharged machining (EDM), meaning that stresses at the base had already been partially relieved during the cut. Indeed, when measuring the average stresses only at the bottom and top of the four faces of the AB sample, a much higher stress of 153.5 MPa was observed at the top compared to 79.75 MPa at the bottom. The same difference could be reported after T5, whereas slight differences could be spotted after

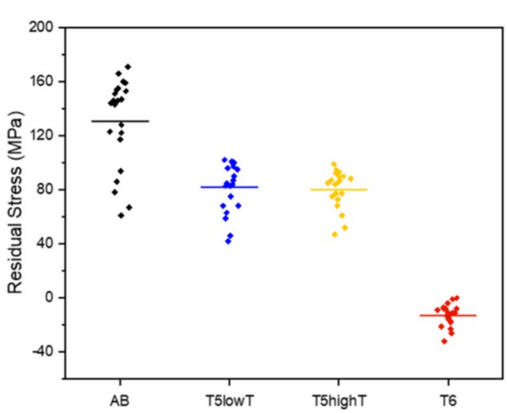

	Residual Stress (MPa)	Standard Deviation	Comparison to AB
AB	130.5	33.1	-
T5LowT	82.1	18.2	-37%
T5HighT	80.3	14.1	-39%
T6	-13.0	8.0	-110%

Figure 11 Characterization of residual stress in AlSi9Cu3 PBF-LB AB and heat-treated alloy (T5LowT, T5HighT, and T6): graphical and numerical results with percentage difference from AB.

T6, thanks to the final homogenization. The more evident peak shift observed in the XRD pattern after T6 is consistent with the stronger microstructural evolution induced by this treatment, as also supported by the DSC and microstructural analyses, together with the more pronounced residual stress relaxation measured in this condition.

Microstructure of the alloy in AB and heat-treated conditions (T5LowT, T5HighT, and T6) are compared in Fig. 12a–d. Microstructural characterization was performed in the MPB zone where, thanks to coarsening, precipitation among cells ascribable to heat treatment is noticeable by FEG-SEM. As previously discussed, the AB microstructure is composed of submicrometric α-Al cells surrounded by an interconnected eutectic Si network (Fig. 12a). The effect of T5LowT treatment on the network is negligible; it still appears as continuous with minor traces of discontinuity, probably due to coalescence. Inside α-Al cells, a partial precipitation of nanometric particles is discernible, as indicated by arrows in Fig. 12b. T5HighT promoted a more pronounced and uniformly distributed precipitation inside cells, with Si network experiencing a partial fragmentation only in some areas and therefore being essentially still interconnected (Fig. 12c). The occurrence of precipitation inside cells during low-temperature annealing was also observed in the literature in case of long-term treatments [24, 25] and ascribed to Al_2Cu precursors (θ') and nanometric Si. EDS analyses performed on heat-treated alloy (Fig. 13a–c suggest that, if compared to the AB condition (Fig. 4), the amount of Si within Al cells slightly raised after direct aging (points 1 and 2 in Figs. 13a,b), thus supporting the occurrence of a precipitation of Si particles. Also, the amount of Cu was enhanced, especially in the T5HighT alloy. These outcomes suggest that precipitation of reinforcing phases can also occur following short-time low-temperature treatment, thus shrinking the time-to-market and reducing energy consumption. On the other hand, T6 samples showed a fully modified microstructure (Fig. 12d). As already observed for other Al-Si alloys [50, 54], the solution treatment fully homogenized the microstructure by promoting the fragmentation and coalescence of the Si network that evolved in a homogeneous distribution of micrometric Si-rich globular particles (ST+WQ treatment, Fig. 7c). Among the globular particles, also homogeneously distributed nanometric particles

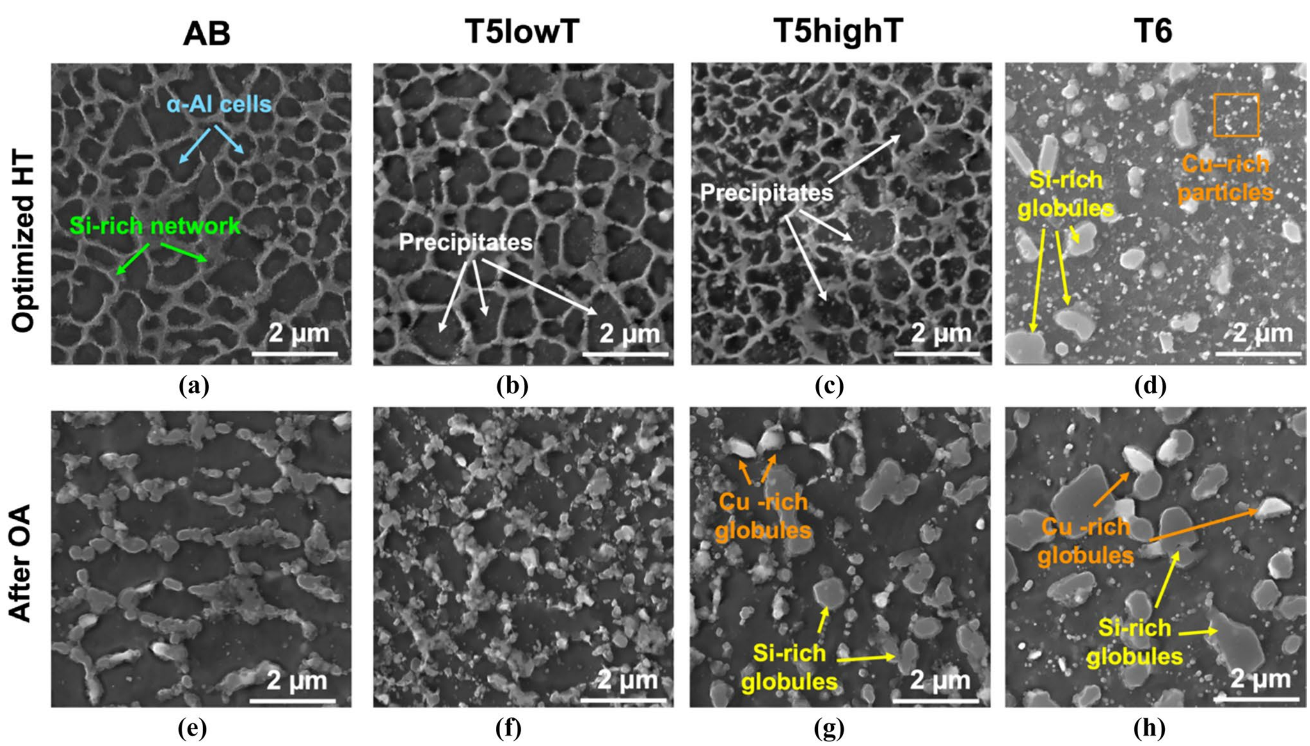

Figure 12 FEG-SEM microstructural analyses on AlSi9Cu3 PBF-LB alloy in the AB and optimized heat-treatment condition defined in Table 3 before overaging **a**, **b**, **c**, **d** and after overaging at 290 °C for 6 h **e**, **f**, **g**, **h**. Micrographs refer to the transversal section (perpendicular to the building direction) and were taken at melt pool borders.

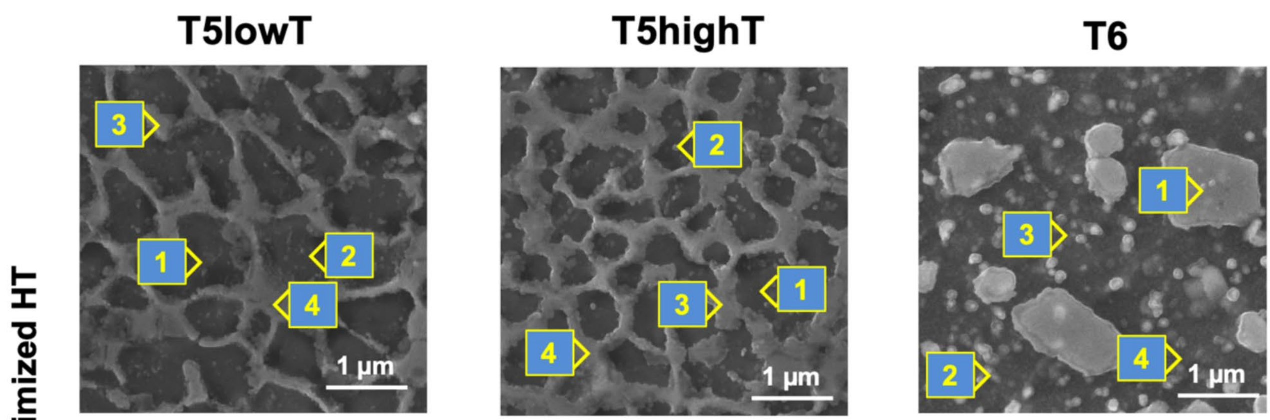

(a) Normalized mass concentration [%]

	Al	Si	Cu	Fe	Mg
1	83.88	12.40	2.87	0.83	0.01
2	87.18	10.18	2.59	0.01	0.04
3	72.62	19.90	4.73	2.74	0.01
4	82.95	11.56	4.15	1.06	0.28

(b) Normalized mass concentration [%]

	Al	Si	Cu	Fe	Mg
1	85.24	9.91	3.13	1.71	0.01
2	83.93	11.08	4.19	0.38	0.42
3	67.16	25.97	4.52	2.05	0.30
4	69.75	24.36	3.56	2.01	0.32

(c) Normalized mass concentration [%]

	Al	Si	Cu	Fe	Mg
1	32.90	64.61	1,73	0.76	0.00
2	90.65	0.88	5.22	3.26	0.00
3	91.21	2.45	4.12	1.96	0.26
4	87.99	5.87	4.57	1.41	0.16

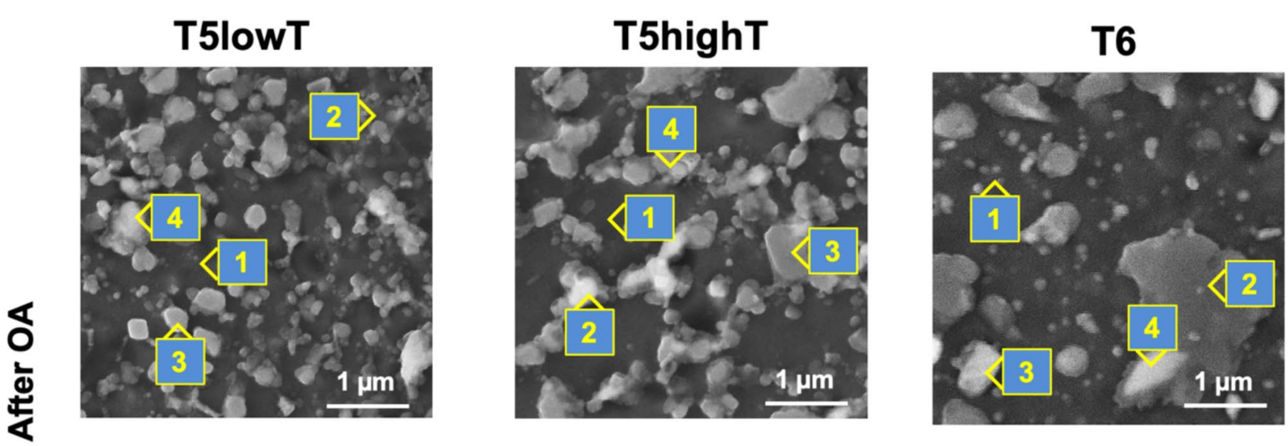

(d) Normalized mass concentration [%]

	Al	Si	Cu	Fe	Mg
1	87.73	10.67	1.60	0.00	0.00
2	85.71	7.00	6.13	0.95	0.21
3	64.56	29.13	5.73	0.58	0.00
4	81.41	11.80	5.75	1.04	0.00

(e) Normalized mass concentration [%]

	Al	Si	Cu	Fe	Mg
1	92.61	2.54	4.60	0.23	0.02
2	82.05	5.84	10.99	1.12	0.00
3	53.77	33.16	9.92	1.76	1.39
4	86.94	7.71	3.59	1.67	0.09

(f) Normalized mass concentration [%]

	Al	Si	Cu	Fe	Mg
1	89.93	5.40	2.40	2.27	0.00
2	19.81	78.43	1.54	0.00	0.22
3	46.09	22.53	31.16	0.00	0.22
4	62.99	3.87	30.96	2.18	0.00

Figure 13 EDS semiquantitative analyses on AlSi9Cu3 PBF-LB in the optimized heat-treatment condition defined in Table 3 before overaging **a**, **b**, **c** and after overaging at 290 °C for 6 h **d**, **e**, **f**. Micrographs refer to the transversal section (perpendicular to the building direction) and were taken at melt pool borders.

were observed, becoming more visible after the aging treatment (full T6 treatment, Fig. 12d). EDS analyses performed in the proximity of these nanometric particles revealed a higher Cu concentration (points 2–4, Fig. 13c) than the nominal alloy composition reported in Table 1, suggesting the possible formation of Cu-rich precipitates. According to the available literature, conventional long-term T6 treatment applied to the

PBF-LB alloy results in the precipitation of θ′′ and coarsening of Fe-rich intermetallic phases, with size ranging up to a few micrometers (needle-like Al_5FeSi, $AlSi_7Cu_2$, and Al_8Fe_5 phases) [23, 24]. In the present work, on the contrary, the T6 treatment has been tailored to the peculiar PBF-LB and specifically devoted to avoid excessive coarsening. Therefore, different outcomes could be expected. XRD analyses (Fig. 10) suggest the formation of different Fe-based phases; however, they also suggest that such phases were small in size and present in a low amount. FEG-SEM observation, in fact, confirmed a microstructure finer than the one reported in the literature, especially in terms of size and distribution of Si-rich globules. Such globules were the only detectable micrometric-sized particles, suggesting that no Fe-based micrometric intermetallic phases were present.

Hence, to gain deeper insight into the fine-scale microstructural features revealed by FEG-SEM observations, nanometric-sized phases were further investigated by TEM to account for the preliminary hardness results obtained for the two T5 treatments and the T6 one.

In Figs. 14 and 15, representative micrographs of the T5LowT, T5HighT, and T6 are reported.

It resulted that a noticeable secondary phase precipitation occurred in the T5LowT condition, and a larger precipitation of the same secondary phase particles was observed in the alloy subjected to T5HighT. These secondary phase particles act as strengthening features for the alloy as they are nanometric size and evenly distributed. In fact, these particles precipitated within the Al grains and sufficiently far from the boundary regions, which were characterized by a significant presence of rounded Si particles. According to the chemical analyses performed by EDS in a quite similar alloy, Roudnická et al. [24] and Fousová et al. [22] revealed that the thin plate-like particles contain Al and Cu, being Al_2Cu-type phases, while the rounded spherical-like ones are Si particles. Both types of particles are within a few tens of nanometers in size. Al_2Cu particles have thickness within few nanometers and lateral size within few tens of nanometers. The T5HighT conditions revealed a slight coarsening of both Si and Al_2Cu particles, which accounted to a coarsening ratio of approximately 40%, from the T5LowT to the T5HighT condition.

The T6 condition revealed the presence of both nanometric spherical-like Si particles and nanometric thin plate-like Al_2Cu particles; these were consistently more abundant in this case than the two T5-treated conditions. In all the three experimental conditions, these strengthening nanometric phases were detected in the grain interior sufficiently far from the alloy grain boundaries and from the intergranular coarse rounded Si particles, which were induced to form during the printing process.

It thus resulted that the larger volume fraction of the thin plate-like particles in the Al grains observed in the T6 condition compared to that observed in the T5HighT and T5LowT sample fully complies with the hardness differences observed.

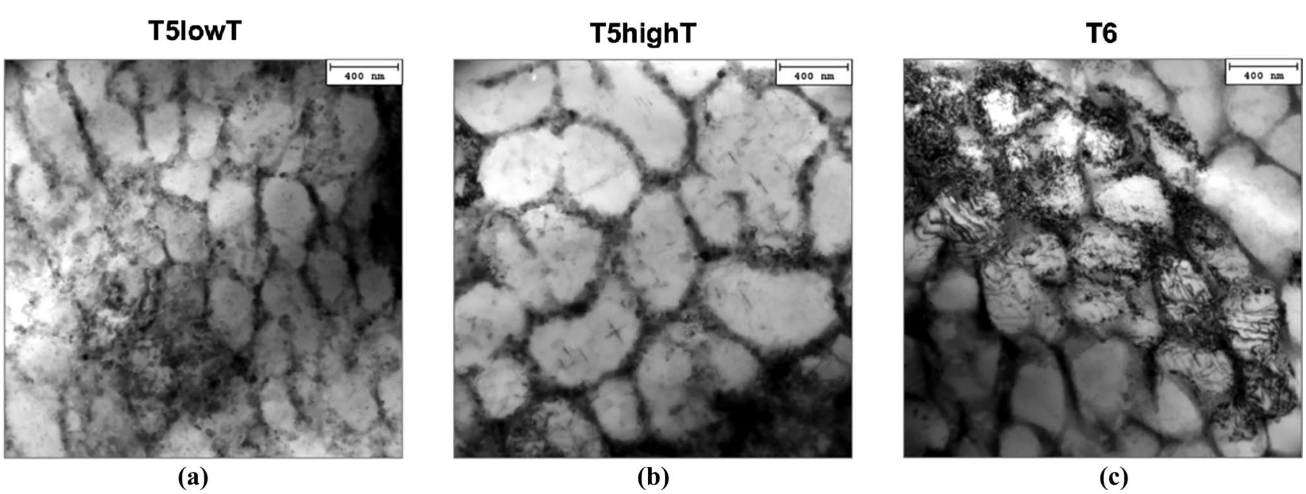

Figure 14 Low-magnification TEM micrographs of AlSi9Cu3 PBF-LB heat-treated alloy: **a** T5LowT; **b** T5HighT; **c** T6.

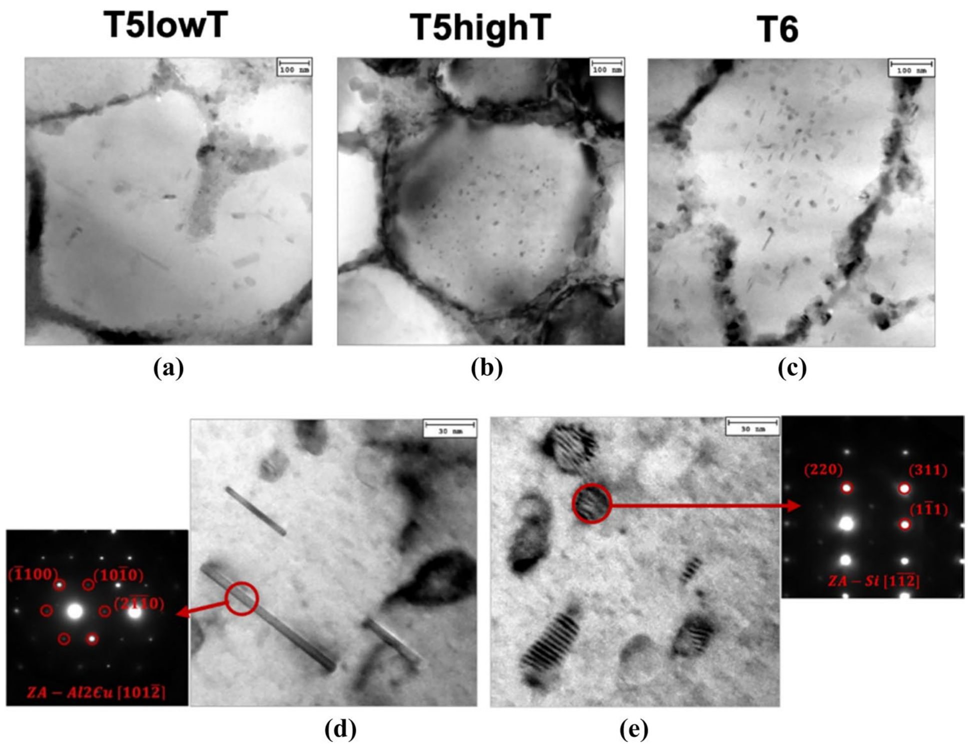

Figure 15 Higher magnification TEM micrographs of AlSi9Cu3 PBF-LB heat-treated alloy: **a** T5LowT; **b** T5HighT; **c** T6; phase identification by SAEDPs, **d** thin plate-like Al_2Cu phase, **e** spherical-like Si phase.

Overaging behavior

Overaging (OA) curves were obtained for all the investigated conditions for an exposure time up to 72 h at 200, 245 and 290 °C (Fig. 16). OA display the evolution in hardness due to the exposure at high temperatures that components, for example, motorbike, automotive, or aerospace ones, might experience during their in-service life. As a first observation, for all the investigated temperatures AB, T5LowT and T5HighT showed a comparable behavior significantly different from the one that characterized the T6 alloy (Fig. 16a–c). Indeed, T6 alloy showed a severe drop in hardness even after a few hours of exposition, especially at higher temperatures (245 and 290 °C) where the hardness plateau was reached after approximately 2 h (Fig. 16e,f). The hardness plateau value for T6 alloy was 80 HB10 (− 42% from peak aged condition). However, it is quite interesting that T6 behavior can be considered replicated for both 245 and 290 °C exposure, thus suggesting that thermal stability was already reached at 245 °C and maintained even at higher temperature. On the other hand, AB, T5LowT, and T5HighT conditions succeeded in preserving a comparable and relatively high hardness even for the most severe overaging conditions. Their minimum recorded hardness is approximately 100 HB10 after 72 h exposure at 290 °C (− 33, − 37, and − 29% from initial hardness for AB, T5LowT, and T5HighT, respectively). For the lowest temperature (200 °C), they even experienced a mild increase in hardness after 30 min exposure (Fig. 16d).

The comparison of the OA behavior of the alloy studied in the present work to the one showed by other Al-Si-Cu-Mg quaternary cast alloys, investigated in previous works [28, 60], allows a more thorough study of this alloy high-temperature response. The comparison is reported in Fig. 17 where representative heat-treated conditions of the AlSi9Cu3 PBF-LB alloy (i.e., T5HighT and T6) are associated with the A354 (AlSi9Cu1.5Mg0.4) and the A357 + Cu (AlSi7Mg0.6 with 1.3 wt% of Cu) cast alloys in the optimized T6 condition (dashed lines in the graphs). The analysis is made between alloys characterized by a similar chemical composition and, most importantly, usually adopted for motorbike and automotive components that face increasing temperatures during their in-service life. From the curves, the most evident result is the outstanding behavior of the AlSi9Cu3 T5HighT condition, which is the only one able to maintain satisfactory hardness values even after long-term exposure at high temperature, without showing any major decrease. By recalling that both AB and T5LowT conditions were characterized by a better thermal stability than T5HighT, it emerges that PBF-LB alloy, AB

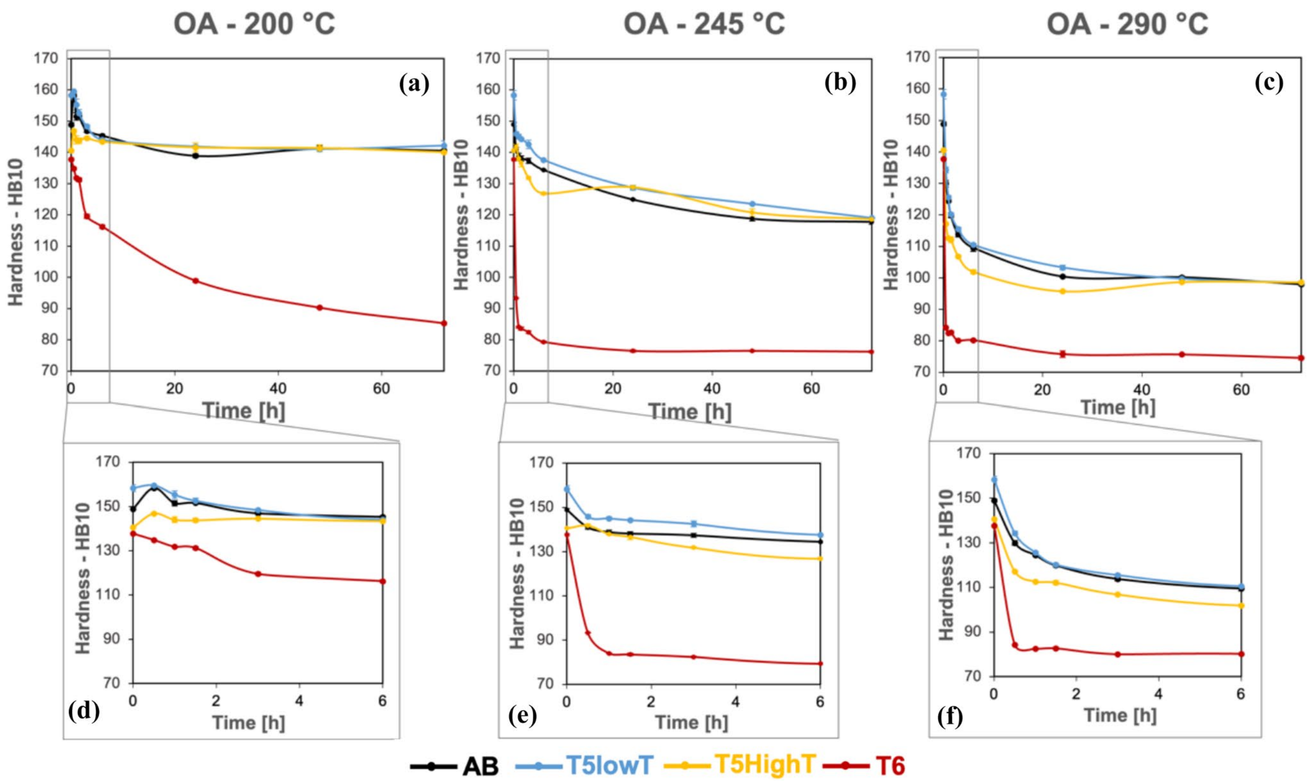

Figure 16 Overaging (OA) curves of the AlSi9Cu3 PBF-LB alloy in AB and optimized heat-treated conditions (T5LowT, T5HighT, and T6 as detailed in Table 3) describing the evolution of hardness (mean value and error bars) as a function of high-temperature exposure up to 72 h at: **a** 200, **b** 245, **c** 290 °C. The insets show magnified views of the 0–6 h range for **d** 200 °C, **e** 245 °C, and **f** 290 °C.

or directly aged, may represent a good candidate for high-temperature applications. On the other hand, T6-treated alloys, both cast and PBF-LB, exhibited a comparable behavior with hardness significantly decreasing with increasing treatment time and temperature. However, it is worth noticing that at 245 and 290 °C, the AlSi9Cu3 PBF-LB alloy showed the most stable behavior and, in case of the highest tested temperature, the hardness value was comparable or even higher than cast alloys.

Results therefore suggest that the high-temperature behavior of both cast and PBF-LB alloys in the T6 state is governed by similar strengthening mechanisms, whereas different mechanisms may contribute to the response of the AB and directly aged PBF-LB alloy. Based on the microstructural analyses so far discussed (Figs. 12–15), it can be inferred that the fine cellular structure with an almost entirely interconnected Si network is the main responsible for the overall excellent thermal stability of AB, T5LowT, and T5HighT conditions. Furthermore, as suggested by XRD and DSC analyses (Figs. 9 and 10), the supersaturation condition characterizing AB and T5LowT gave additional support, if compared to T5HighT, especially for short-time exposure (Fig. 16d–f). Fine cellular structure and supersaturation are not present in the T6 state. Therefore, the precipitation of strengthening secondary phases, which is more pronounced in the T6 alloy than in the T5 condition, is presumably the dominant mechanism governing the high-temperature response. Thermal resistance of T6 cast alloys is explained by the presence of Cu-based phases (θ-Al_2Cu and eventually Q-$Al_5Cu_2Mg_8Si_6$) being stable for temperatures up to 300 °C [31]. Therefore, based on the OA curves, it could be inferred that an analogous mechanism dominates also the PBF-LB T6 alloy. θ-Al_2Cu phases have indeed been observed also in the T6 alloy studied in the present work, in the form of plate-like precipitates within Al cells, along with spherical Si precipitates (Fig. 15). Since TEM analyses did not reveal the presence of Q-phase or Fe-based particles, the improved thermal stability of the PBF-LB alloy at

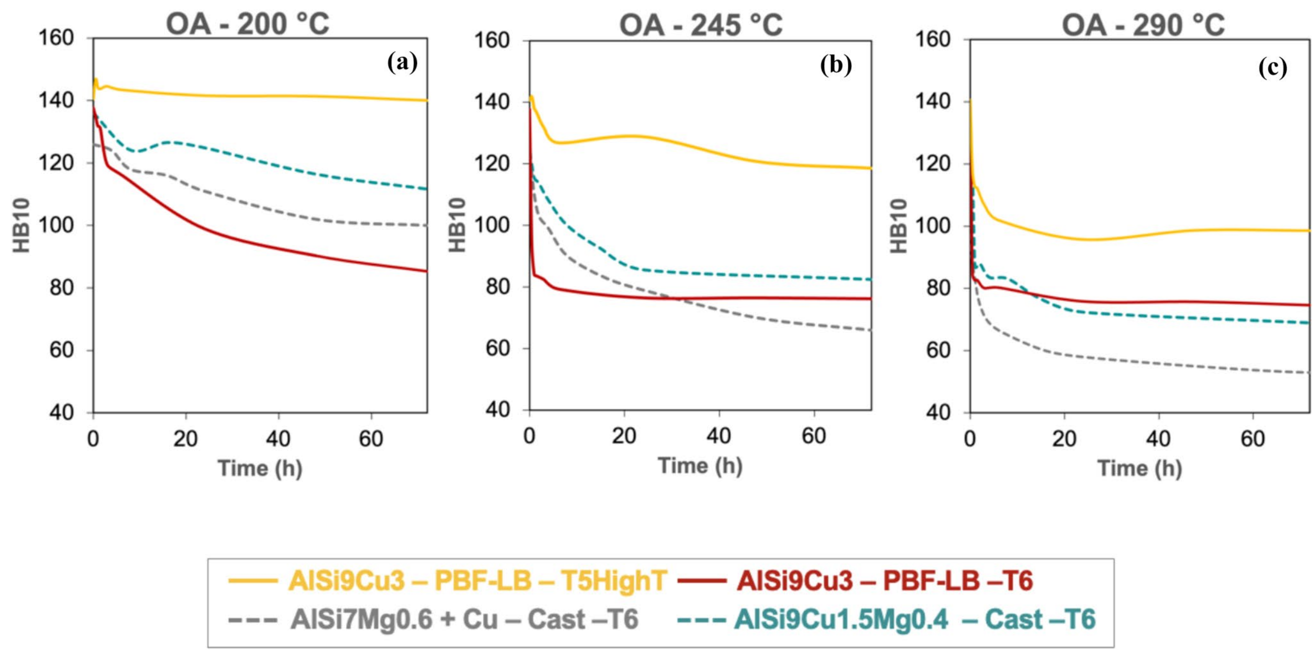

Figure 17 Comparison of overaging (OA) behavior of the AlSi9Cu3 PBF-LB alloy studied in the present work and conventional Al–Si–Cu–Mg cast alloys previously studied by the authors [28, 60]. OA curves are obtained at: **a** 200, **b** 245, and **c** 290 °C for all the considered alloys.

higher temperatures, compared with the cast alloys, may be attributed to the homogeneous dispersion of Si nanoparticles. These outcomes were also corroborated by microstructural analyses carried out on samples overaged for 6 h at 290 °C (Fig. 12e–h). This OA condition was selected as representative because all the investigated heat-treatment states reached a hardness plateau at this point, thereby minimizing the possible effects of excessive coarsening due to prolonged exposure. Passing from AB to T5LowT and T5HighT, the effect of high-temperature exposure on the cellular structure becomes progressively more pronounced. OA gradually induced the coarsening and eventually the breakdown of the cells' borders, evolved from an almost interconnected network into globular particles. If the network before OA was continuous, like in the case of AB, after OA traces of the cellular structure can still be recognized (Fig. 12e). Otherwise, if the network was modified by T5 treatment, especially if performed at high temperature, the modification of the cellular microstructure is much more evident (Fig. 12g). The evolution of the Si network during overaging supports the hypothesis that this microstructural feature plays a major role in providing thermal stability. EDS analyses on OA conditions (Fig. 13d–f) showed that among the fragmented and globalized Si network, also Cu-rich particles were formed, presumably due to the coalescence of smaller particles. On the other hand, OA did not significantly modify the morphology of the T6 microstructure, but a significant coarsening of both Si-rich and Cu-rich particles was observed (Fig. 12h). In particular, as also suggested by EDS analyses in Fig. 13f, nanometric Cu-rich particles evolved in micrometric globules after OA. This outcome corroborates the hypothesis that coarsening of reinforcing particles is the main responsible for the high-temperature response of the alloy in the T6 state.

Conclusions

This research aims to investigate the aging and overaging behavior of the AlSi9Cu3 alloy produced by powder bed fusion additive manufacturing (PBF-LB) by correlating mechanical (hardness) measurements with a comprehensive microstructural study. The study seeks to optimize post-processing heat treatments tailored to the peculiar PBF-LB microstructure and to assess the high-temperature response of the optimized conditions. Two strategies were investigated: short-term direct aging treatments for strengthening

(T5LowT) or stress relieving (T5HighT), and a tailored T6 treatment. The following conclusions can be drawn:

- As-built (AB) alloy is characterized by a high hardness (approximately 150 HB10) by reason of the extremely fine cellular solidification structure and supersaturation condition resulting from the PBF-LB process. Concurrently, the alloy in the AB state is also characterized by significant tensile residual stress.

- Direct aging (T5) treatments are enabled by the supersaturation of AB alloy, and both short-term treatments induced a homogeneous precipitation of Si nanoparticles and θ-Al_2Cu phases, with peak aging obtained at the low-temperature treatment (T5LowT, + 7% from AB) where reinforcing particles were finer. The high-temperature treatment (T5HighT) produced an increased precipitation of Si and θ-Al_2Cu phases but also their coarsening, leading to an overall slight decrease in hardness that could enhance ductility (− 7% from AB). However, both T5 preserved the peculiar fine cellular structure of the AB state and succeeded in decreasing the tensile residual stress by approximately 40%.
- Tailored T6 treatment, optimized to avoid excessive coarsening, induced a complete transformation in the microstructure. Solution treatment converted the interconnected cellular network of the AB alloy into a homogeneous distribution of submicrometric globular Si-rich particles within the Al matrix. Along with the loss of the supersaturation condition, microstructural changes led to a drop in hardness (approximately − 30% from AB). However, the following aging state led to hardness increase, up to a value comparable to T5HighT, thanks to the precipitation of mainly θ-Al_2Cu phases. Furthermore, complete relief of residual stress was evidenced in T6 samples.
- Exposure at high temperature led to an overall decrease in alloy hardness for all the considered conditions; however, the decrease was significantly more accentuated and accelerated in case of T6 samples, whose behavior is comparable to previously investigated cast alloys. Microstructural analyses suggest that the fine cellular structure of AB and T5 states is the most effective strengthening mechanism to face high temperatures.

Acknowledgements

The authors would like to thank Lorenzo Maria Zenoni for his valuable support during the experimental campaign.

Funding

Open access funding provided by Alma Mater Studiorum - Università di Bologna within the CRUI-CARE Agreement. This research was financed by the European Union—NextGenerationEU (National Sustainable Mobility Center CN00000023, Italian Ministry of University and Research Decree n. 1033–17/06/2022, Spoke 11—Innovative Materials and Lightweighting). The opinions expressed are those of the authors only and should not be considered as representative of the European Union or the European Commission's official position. Neither the European Union nor the European Commission can be held responsible for them.

Data availability

Data will be available on reasonable request from the authors.

Declarations

Competing interests The authors declare that they have no known competing financial interests or personal relationships that could have appeared to influence the work reported in this paper.

References

[1] Yu X, LeBlanc S, Sandhu N, Wang L, Wang M, Zheng M (2024) Decarbonization potential of future sustainable propulsion—a review of road transportation. Energy Sci Eng 12:438–455. https://doi.org/10.1002/ese3.1434

[2] Antonacci A, Matheis R, Del Pero F, Thirunavukkarasu D, Delogu M (2025) Design of experiments framework for performance and environmental assessment in automotive context. Proc Inst Mech Eng D J Automob Eng 239:464–488. https://doi.org/10.1177/09544070231206880

[3] Antonacci A, Del Pero F, Baldanzini N, Delogu M (2022) Holistic eco-design tool within automotive field. IOP Conf Ser Mater Sci Eng 1214:012045. https://doi.org/10.1088/1757-899X/1214/1/012045

[4] Czerwinski F (2021) Current trends in automotive lightweighting strategies and materials. Materials 14:6631. https://doi.org/10.3390/ma14216631

[5] Busarac N, Adamovic D, Grujovic N, Zivic F (2022) Lightweight materials for automobiles. IOP Conf Ser Mater Sci Eng 1271:012010. https://doi.org/10.1088/1757-899X/1271/1/012010

[6] Candela A, Sandrini G, Gadola M, Chindamo D, Magri P (2024) Lightweighting in the automotive industry as a measure for energy efficiency: review of the main materials and methods. Heliyon 10:e29728. https://doi.org/10.1016/j.heliyon.2024.e29728

[7] Moura B, Monteiro H (2025) Current development of the metal additive manufacturing sustainability—a systematic review. Environ Impact Assess Rev 112:107778. https://doi.org/10.1016/j.eiar.2024.107778

[8] Patel S, Liu Y, Siddique Z, Ghamarian I (2024) Metal additive manufacturing: principles and applications. J Manuf Process 131:1179–1201. https://doi.org/10.1016/j.jmapro.2024.09.101

[9] Sala D, Richert M (2025) Perspectives of additive manufacturing in 5.0 industry. Materials (Basel) 18:429. https://doi.org/10.3390/ma18020429

[10] Singh R, Gupta A, Tripathi O, Srivastava S, Singh B, Awasthi A, Rajput SK, Sonia P, Singhal P, Saxena KK (2020) Powder bed fusion process in additive manufacturing: an overview. Mater Today Proc 26:3058–3070. https://doi.org/10.1016/j.matpr.2020.02.635

[11] Chandra S, Radhakrishnan J, Huang S, Wei S, Ramamurty U (2025) Solidification in metal additive manufacturing: challenges, solutions, and opportunities. Prog Mater Sci 148:101361. https://doi.org/10.1016/j.pmatsci.2024.101361

[12] Liu Z, Zhao D, Wang P, Yan M, Yang C, Chen Z, Lu J, Lu Z (2022) Additive manufacturing of metals: microstructure evolution and multistage control. J Mater Sci Technol 100:224–236. https://doi.org/10.1016/j.jmst.2021.06.011

[13] Yang X, Li R, Yuan T, Ke L, Bai J, Yang K (2025) A comprehensive overview of additive manufacturing aluminum alloys: classifications, structures, properties and defects elimination. Mater Sci Eng A 919:147464. https://doi.org/10.1016/j.msea.2024.147464

[14] Kotadia HR, Gibbons G, Das A, Howes PD (2021) A review of laser powder bed fusion additive manufacturing of aluminium alloys: microstructure and properties. Addit Manuf 46:102155. https://doi.org/10.1016/j.addma.2021.102155

[15] Sanna F, Fabrizi A, Ferraro S, Timelli G, Ferro P, Bonollo F (2013) Multiscale characterisation of AlSi9Cu3(Fe) die casting alloys after Cu, Mg, Zn and Sr addition. Metallurgia Italiana 105:13–24

[16] Timelli G, Fabrizi A (2014) The effects of microstructure heterogeneities and casting defects on the mechanical properties of high-pressure die-cast AlSi9Cu3(Fe) alloys. Metall Mater Trans A 45:5486–5498. https://doi.org/10.1007/s11661-014-2515-7

[17] Javidani M, Larouche D (2014) Application of cast Al–Si alloys in internal combustion engine components. Int Mater Rev 59:132–158. https://doi.org/10.1179/1743280413Y.0000000027

[18] Anderson K, Weritz J, Kaufman JG (eds) (2019) Properties and selection of aluminum alloys. ASM International. https://doi.org/10.31399/asm.hb.v02b.9781627082105

[19] Sjölander E, Seifeddine S (2010) The heat treatment of Al–Si–Cu–Mg casting alloys. J Mater Process Technol 210:1249–1259. https://doi.org/10.1016/j.jmatprotec.2010.03.020

[20] ASTM B917/B917M—12, (2020) Standard Practice for Heat Treatment of Aluminum-Alloy Castings from All Processes, ASTM International: West Conshohocken, PA, USA, https://doi.org/10.1520/B0917_B0917M-12R20

[21] Suchy J, Pantelejev L, Palousek D, Koutny D, Kaiser J (2020) Processing of AlSi9Cu3 alloy by selective laser melting. Powder Metall 63:197–211. https://doi.org/10.1080/00325899.2020.1792675

[22] Fousova M, Dvorsky D, Vronka M, Vojtech D, Lejcek P (2018) The use of selective laser melting to increase

the performance of AlSi9Cu3Fe alloy. Materials (Basel) 11:1918. https://doi.org/10.3390/ma11101918

[23] Fiocchi J, Biffi CA, Tuissi A (2020) Selective laser melting of high-strength primary AlSi9Cu3 alloy: processability, microstructure, and mechanical properties. Mater Des 191:108581. https://doi.org/10.1016/j.matdes.2020.108581

[24] Roudnická M, Molnárová O, Dvorský D, Křivský L, Vojtěch D (2020) Specific response of additively manufactured AlSi9Cu3Fe alloy to precipitation strengthening. Met Mater Int 26:1168–1181. https://doi.org/10.1007/s12540-019-00504-y

[25] Fiocchi J, Colombo C, Vergani LM, Fabrizi A, Timelli G, Tuissi A, Biffi CA (2021) Heat treatments for stress relieving AlSi9Cu3 alloy produced by laser powder bed fusion. Materials (Basel) 14:4184. https://doi.org/10.3390/ma14154184

[26] Ponnusamy P, Rahman Rashid RA, Masood SH, Ruan D, Palanisamy S (2020) Mechanical properties of SLM-printed aluminium alloys: a review. Materials (Basel) 13:4301. https://doi.org/10.3390/ma13194301

[27] Mondolfo LF (1976) Aluminum alloys. Elsevier. https://doi.org/10.1016/C2013-0-04239-9

[28] Ceschini L, Messieri S, Morri A, Seifeddine S, Toschi S, Zamani M (2020) Effect of Cu addition on overaging behaviour, room and high temperature tensile and fatigue properties of A357 alloy. Trans Nonferrous Met Soc China 30:2861–2878. https://doi.org/10.1016/S1003-6326(20)65427-9

[29] Ceschini L, Morri A, Toschi S, Johansson S, Seifeddine S (2015) Microstructural and mechanical properties characterization of heat treated and overaged cast A354 alloy with various SDAS at room and elevated temperature. Mater Sci Eng A 648:340–349. https://doi.org/10.1016/j.msea.2015.09.072

[30] Ceschini L, Morri A, Morri A, Toschi S, Johansson S, Seifeddine S (2015) Effect of microstructure and overaging on the tensile behavior at room and elevated temperature of C355–T6 cast aluminum alloy. Mater Des 83:626–634. https://doi.org/10.1016/j.matdes.2015.06.031

[31] Farkoosh AR, Pekguleryuz M (2015) Enhanced mechanical properties of an Al–Si–Cu–Mg alloy at 300 °C: effects of Mg and the Q-precipitate phase. Mater Sci Eng A 621:277–286. https://doi.org/10.1016/j.msea.2014.10.080

[32] Shower P, Morris JR, Shin D, Radhakrishnan B, Allard LF, Shyam A (2019) Temperature-dependent stability of θ'-Al2Cu precipitates investigated with phase field simulations and experiments. Materialia 5:100185. https://doi.org/10.1016/j.mtla.2018.100185

[33] Farkoosh AR, Javidani M, Hoseini M, Larouche D, Pekguleryuz M (2013) Phase formation in as-solidified and heat-treated Al–Si–Cu–Mg–Ni alloys: thermodynamic assessment and experimental investigation for alloy design. J Alloys Compd 551:596–606. https://doi.org/10.1016/j.jallcom.2012.10.182

[34] ASTM E3–11(2017), Standard Guide for Preparation of Metallographic Specimens, ASTM International: West Conshohocken, PA, USA, https://doi.org/10.1520/E0003-11R17

[35] Warmuzek M (2004) Metallographic techniques for aluminum and its alloys. In: Vander Voort GF (ed) Metallogr. microstruct. ASM International, pp 711–751. https://doi.org/10.31399/asm.hb.v09.a0003769

[36] ASTM E10–18, (2018) Standard Test Method for Brinell Hardness of Metallic Materials, ASTM International: West Conshohocken, PA, USA, https://doi.org/10.1520/E0010-23

[37] Samuel AM, Doty HW, Valtierra S, Samuel FH (2013) Effect of Mg addition of microstructure of 319 type alloys. Int J Cast Met Res 26:354–363. https://doi.org/10.1179/1743133613Y.0000000071

[38] Samuel FH (1998) Incipient melting of Al5Mg8Si6Cu2 and Al_2Cu intermetallics in unmodified and strontium-modified Al–Si–Cu–Mg (319) alloys during solution heat treatment. J Mater Sci 33:2283–2297. https://doi.org/10.1023/A:1004383203476

[39] Sigworth GK (2016) Heat treatment of aluminum alloy castings. In: Totten GE (ed) Heat treat. nonferrous alloys. ASM International, pp 274–288. https://doi.org/10.31399/asm.hb.v04e.a0006264

[40] Trevisan F, Calignano F, Pakkanen J, Ambrosio E, Lombardi M, Pavese M, Manfredi D, Fino P (2016) Effects of heat treatments on a357 alloy produced by selective laser melting, European Congress and Exhibition on Powder Metallurgy, European PM Conference Proceedings,1–6

[41] Pereira JC, Gil E, Solaberrieta L, San Sebastián M, Bilbao Y, Rodríguez PP (2020) Comparison of AlSi7Mg0.6 alloy obtained by selective laser melting and investment casting processes: Microstructure and mechanical properties in as-built/as-cast and heat-treated conditions. Mater Sci Eng A 778:139124. https://doi.org/10.1016/j.msea.2020.139124zz

[42] Balducci E, Ceschini L, Morri A, Morri A (2017) EN AW-4032 T6 piston alloy after high-temperature exposure: residual strength and microstructural features. J Mater Eng Perform 26:3802–3812. https://doi.org/10.1007/s11665-017-2835-z

[43] Aboulkhair NT, Everitt NM, Ashcroft I, Tuck C (2014) Reducing porosity in AlSi10Mg parts processed by selective laser melting. Addit Manuf 1–4:77–86. https://doi.org/10.1016/j.addma.2014.08.001

[44] Casati R, Coduri M, Checchia S, Vedani M (2021) Insight into the effect of different thermal treatment routes on the microstructure of AlSi7Mg produced by laser powder bed fusion. Mater Charact 172:110881. https://doi.org/10.1016/j.matchar.2021.110881

[45] Thijs L, Kempen K, Kruth J-P, Van Humbeeck J (2013) Fine-structured aluminium products with controllable texture by selective laser melting of pre-alloyed AlSi10Mg powder. Acta Mater 61:1809–1819. https://doi.org/10.1016/j.actamat.2012.11.052

[46] Aboulkhair NT, Everitt NM, Maskery I, Ashcroft I, Tuck C (2017) Selective laser melting of aluminum alloys. MRS Bull 42:311–319. https://doi.org/10.1557/mrs.2017.63

[47] Luiggi A. NJ (2010) A preliminary study of the phase transformations in rolled Al–Fe–Si alloy. Metall Mater Trans A 41(13):3271–3275. https://doi.org/10.1007/s11661-010-0496-8

[48] Laleh M, Sadeghi E, Revilla RI, Chao Q, Haghdadi N, Hughes AE, Xu W, De Graeve I, Qian M, Gibson I, Tan MY (2023) Heat treatment for metal additive manufacturing. Prog Mater Sci 133:101051. https://doi.org/10.1016/j.pmatsci.2022.101051

[49] Ponnusamy P, Rahman Rashid RA, Masood SH, Ruan D, Palanisamy S (2020) Mechanical properties of SLM-printed aluminium alloys: a review. Materials 13:4301. https://doi.org/10.3390/ma13194301

[50] Di Egidio G, Ceschini L, Morri A, Martini C, Merlin M (2022) A novel T6 rapid heat treatment for AlSi10Mg alloy produced by laser-based powder bed fusion: comparison with T5 and conventional T6 heat treatments. Metall Mater Trans B 53:284–303. https://doi.org/10.1007/s11663-021-02365-6

[51] Tonelli L, Liverani E, Di Egidio G, Fortunato A, Morri A, Ceschini L (2023) On the role of microstructure and defects in the room and high-temperature tensile behavior of the PBF-LB A357 (AlSi7Mg) alloy in as-built and peak-aged conditions. Materials 16:2721. https://doi.org/10.3390/ma16072721

[52] Chen M, Xing S, Li J, He J, Lu Y, Jiang C, Ji V (2021) Surface residual stress and microstructure evolutions of Hastelloy X alloy after severe shot peening. Vacuum 187:110136. https://doi.org/10.1016/j.vacuum.2021.110136

[53] Yang Y, Yang M, He C, Qi F, Wang D, Peng S, Shuai C (2021) Rare earth improves strength and creep resistance of additively manufactured Zn implants. Compos Part B Eng 216:108882. https://doi.org/10.1016/j.compositesb.2021.108882

[54] Tonelli L, Liverani E, Morri A, Ceschini L (2021) Role of direct aging and solution treatment on hardness, microstructure and residual stress of the A357 (AlSi7Mg0.6) alloy produced by powder bed fusion. Metall Mater Trans B 52:2484–2496. https://doi.org/10.1007/s11663-021-02179-6

[55] Clement CD, Masson J, Kabir AS (2022) Effects of heat treatment on microstructure and mechanical properties of AlSi10Mg fabricated by selective laser melting process. J Manuf Mater Process 6:52. https://doi.org/10.3390/jmmp6030052

[56] Maleki E, Bagherifard S, Guagliano M (2023) Correlation of residual stress, hardness and surface roughness with crack initiation and fatigue strength of surface treated additive manufactured AlSi10Mg: experimental and machine learning approaches. J Mater Res Technol 24:3265–3283. https://doi.org/10.1016/j.jmrt.2023.03.193

[57] Fiocchi J, Tuissi A, Biffi CA (2021) Heat treatment of aluminium alloys produced by laser powder bed fusion: a review. Mater Des 204:109651. https://doi.org/10.1016/j.matdes.2021.109651

[58] Delroisse P, Jacques PJ, Maire E, Rigo O, Simar A (2017) Effect of strut orientation on the microstructure heterogeneities in AlSi10Mg lattices processed by selective laser melting. Scr Mater 141:32–35. https://doi.org/10.1016/j.scriptamat.2017.07.020

[59] Bagherifard S, Beretta N, Monti S, Riccio M, Bandini M, Guagliano M (2018) On the fatigue strength enhancement of additive manufactured AlSi10Mg parts by mechanical and thermal post-processing. Mater Des 145:28–41. https://doi.org/10.1016/j.matdes.2018.02.055

[60] Toschi S (2018) Optimization of A354 Al–Si–Cu–Mg alloy heat treatment: effect on microstructure, hardness, and tensile properties of peak aged and overaged alloy. Metals 8:961. https://doi.org/10.3390/met8110961

Publisher's Note Springer Nature remains neutral with regard to jurisdictional claims in published maps and institutional affiliations.